Supplementary Information For

Tailoring Photoluminescence and Multifunctionalities of Lanthanide Coordination Complexes Employing the Ligand-Controlled Aggregation States

Jun Wang [1†*], Qianbo Zhang [1†], Zhiming Chen [1], Xin Lan [1], Wenjing Shi [1], Zhiqiang Li [2*]

[1] School of Chemistry and Materials Science, Guizhou Normal University, Guiyang 550001, China.

[2] Chemical Engineering and Technology, Hebei University of Technology, Tianjin 300130, China.

Corresponding Author

* J. Wang, beyoundme@126.com; Z. Li, zhiqiangli@hebut.edu.cn

† Jun Wang and Qianbo Zhang contributed equally.

Contents

1. *Experimental section*

The synthetic routes of reference ligand (**RL**, N'-([2,2':6',2''-terpyridin]-4'-yl)propane-1,3-diamine) and target ligand (**TL**, 2-(3-([2,2':6',2''-terpyridin]-4'-ylamino)propyl)-1H-benzo[de]isoquinoline-1,3(2H)-dione) are listed in **Scheme S1**.

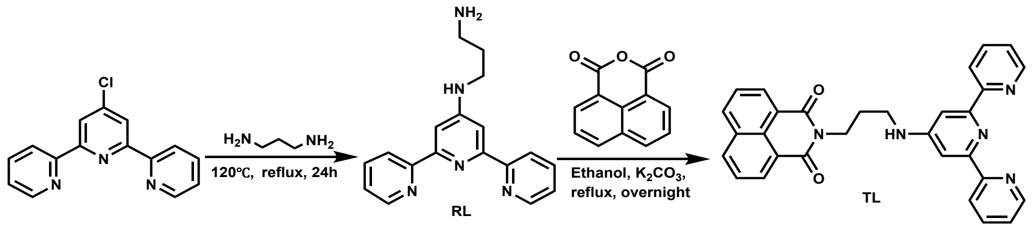

Scheme S1. The synthetic routes of **RL** and **TL**

Synthesis of RL: **RL** was synthesized according to a previously reported synthetic procedure [S1].

Synthesis of TL: the detailed synthesis of **TL** was described as follows according to McCluskey's report [S2]. Using anhydrous potassium carbonate as a catalyst, a mixture of **RL** (100 mg, 0.33 mmol), 1,8-naphthaleneanhydride (70 mg, 0.35 mmol), and 60 mL absolute ethanol was stirred under 80 °C overnight. After the solvent was cooled to room temperature, the precipitate filter was washed with hot water and dried. The residue was purified by recrystallization from ethanol and water to obtain **TL** as a white powder. Yield: 105 mg (66%). **TL** was well characterized by NMR, HRMS, and IR spectra. ^{1}H NMR ($CDCl_3$, 400 MHz) δ 8.68-8.59 (m, 6H), 8.24-8.22 (d, 2H), 7.85-7.73 (m, 6H), 7.32-7.29 (t, 2H), 5.28-5.25 (t, 1H), 4.37-4.34 (t, 2H), 3.49-3.44 (q, 2H), 2.16-2.10 (m, 2H); ^{13}C NMR ($CDCl_3$, 100 MHz) δ 164.70, 157.01, 156.01, 155.40, 148.97, 136.83, 134.29, 131.73, 131.62, 128.33, 127.15, 123.58, 122.60, 121.48, 104.89, 39.77, 37.72, 27.60; HRMS-ESI m/z (%): Calculated for $C_{30}H_{23}N_5O_2$ $[M + H]^+$: 486.1925;

Found: 486.1900; IR: 3372 cm^{-1} (Ar-NH-); 3057 cm^{-1} (Ar-H); 2963, 2846 cm^{-1} (-CH_2-); 1699 cm^{-1} (-C=O); 1653 cm^{-1} (C=N), 1582 cm^{-1} (C=C), 1265 cm^{-1} (C-C-N).

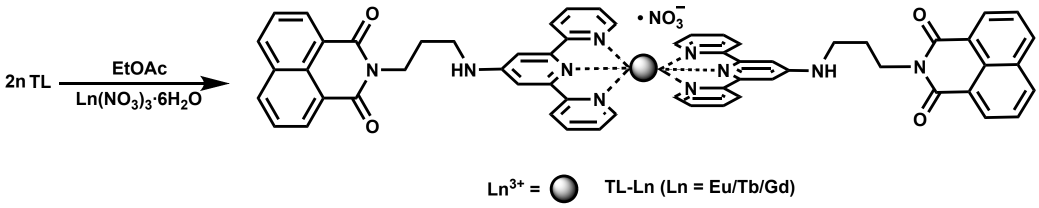

Scheme S2. The synthetic routes of **TL-Ln (Ln = Eu/Tb/Gd)**

Synthesis of TL-Eu/Tb/Gd and RL-Eu/Tb (Scheme S2): To a stirred 0.11 mmol **TL/RL** in 30 mL ethyl acetate, 0.05 mmol $Ln(NO_3)_3 \cdot 6H_2O$ (Ln = Eu^{3+}, Tb^{3+}, Gd^{3+}) in 6 mL ethyl acetate was added and reacted for 24 h at 40 °C. White precipitates were obtained by filtration and washed with excess ethyl acetate. ICP and EA (%) calculated for [$C_{60}H_{46}N_{13}O_{13}Eu$]: Eu 11.68; C 54.99; H 3.54; N 13.90. Found: Eu 11.81; C 52.68; H 3.72; N 13.78. ICP and EA (%) calculated for [$C_{60}H_{46}N_{13}O_{13}Tb$]: Tb 12.08; C 54.76; H 3.52; N 13.84. Found: Tb 12.68; C 53.21; H 3.37; N 13.11. ICP and EA (%) calculated for [$C_{60}H_{46}N_{13}O_{13}Gd$]: Gd 11.96; C 54.83; H 3.53; N 13.85. Found: Gd 12.04; C 52.94; H 3.26; N 12.54.

Determination of the association constant

The association constant (K_a) value was calculated based on the fluorescent titration data. K_a for the formation of a complex between **TL** and Eu^{3+}/Tb^{3+} or other metal ions (*Mi*) can be described by following expression (3):

$$K_a = \frac{[2TL \cdot Mi]}{[TL]^2[Mi]} \qquad (3)$$

where [**TL**], [Mi], [2TL·Mi] are the equilibrium concentration of **TL**, metal ions including Eu^{3+}/Tb^{3+} and 2TL·Mi, $\boldsymbol{K_a}$ can be obtained according to the reported method [S3] by the equation (4).

$$y = \frac{x}{2 \times a \times b \times (1-x)^2} + \frac{x \times b}{2} \qquad (4)$$

Here, x is $(A - A_0)/(A_{max} - A_0)$, y is the concentration of metal ions, a is the K_a, and b is the concentration of **TL**, respectively.

The calculation for the limit of detection

The limit of detection (LOD) was calculated by the following equation (5) according to the previous literature [S4].

$$LOD = (3 \times \sigma)/Slope \qquad (5)$$

Where LOD and σ represent the limit of detection and standard deviation of the blank (**S**).

$$\sigma = \sqrt{\sum (A(I) - A1(I1))^2 / (N-1)}$$

Where A/I is the absorbance/intensity of **TL/TL-Eu** in the absence of analytes, **A1/I1** is the average of A/I. N = 10.

2. Supporting figures

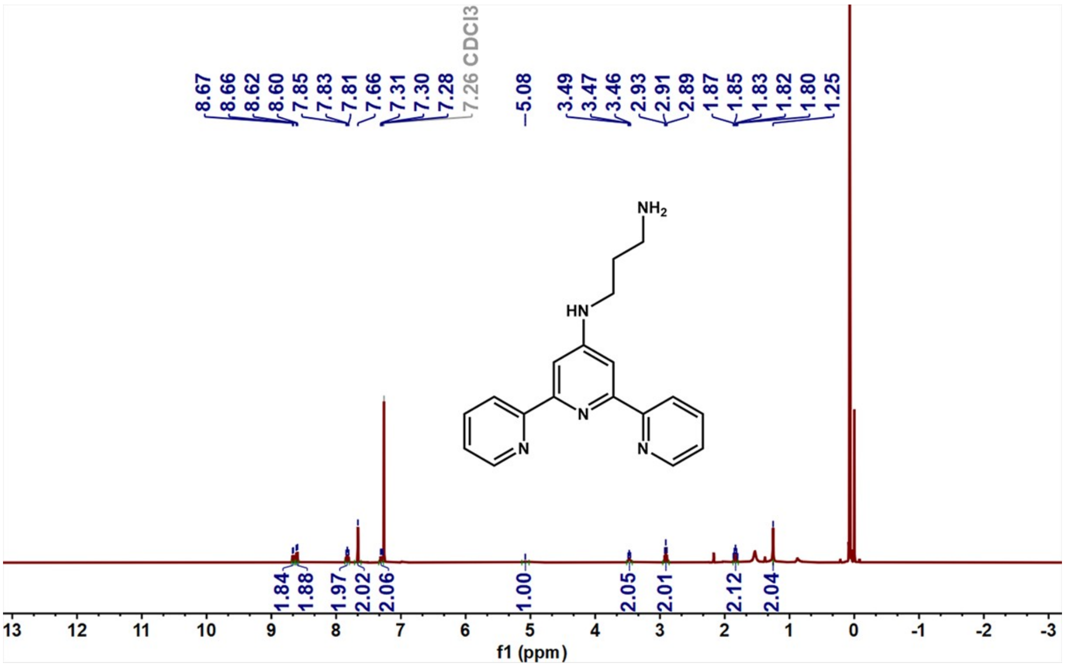

Figure S1 ^{1}H NMR spectrum (400 MHz, 25 °C) of **RL** in $CDCl_3$.

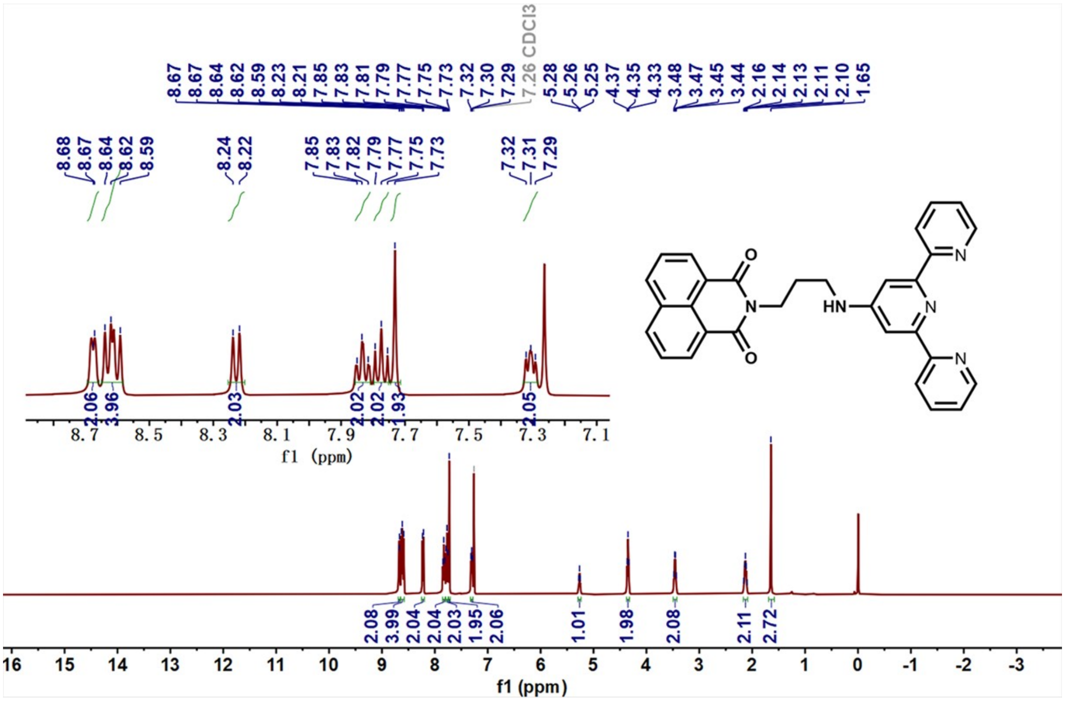

Figure S2 ^{1}H NMR spectrum (400 MHz, 25 °C) of **TL** in $CDCl_3$.

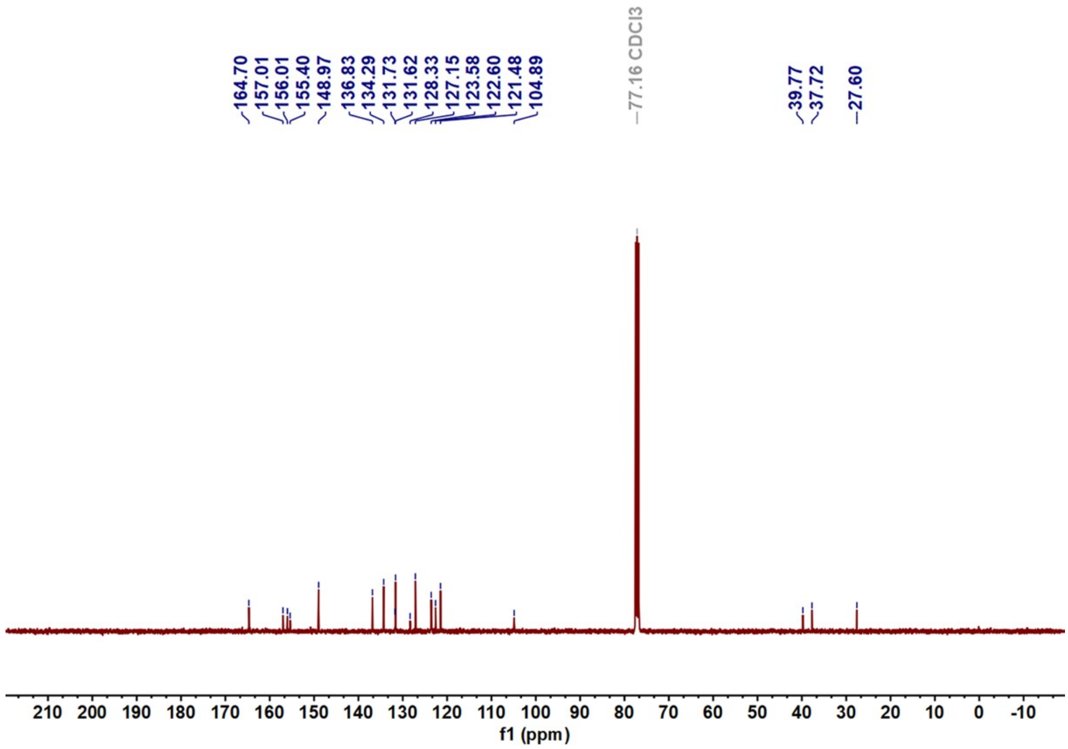

Figure S3 ^{13}C NMR spectrum (100 MHz, 25 °C) of **TL** in $CDCl_3$.

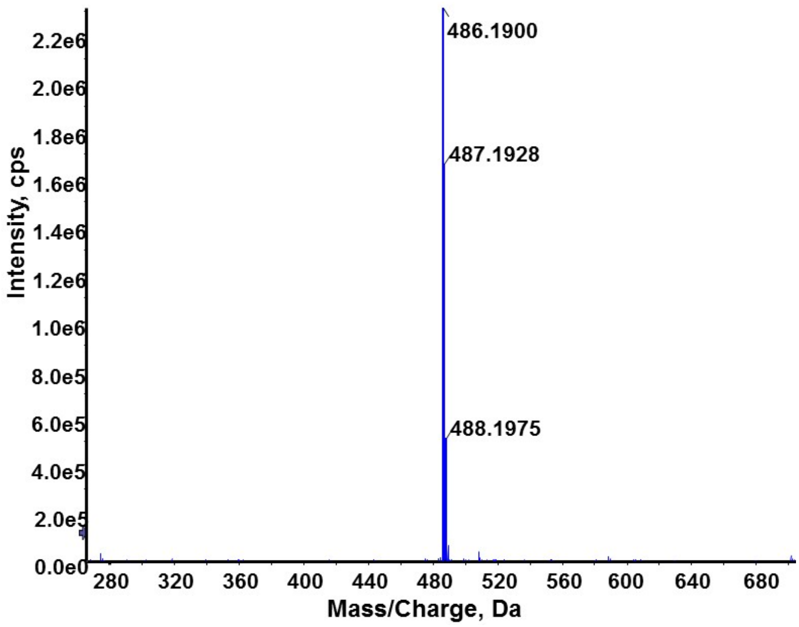

Figure S4 ESI-MS spectrum of **TL,** Calcd. For $C_{30}H_{23}N_5O_2$ $[M + H]^+$: 486.1925; Found: 486.1900.

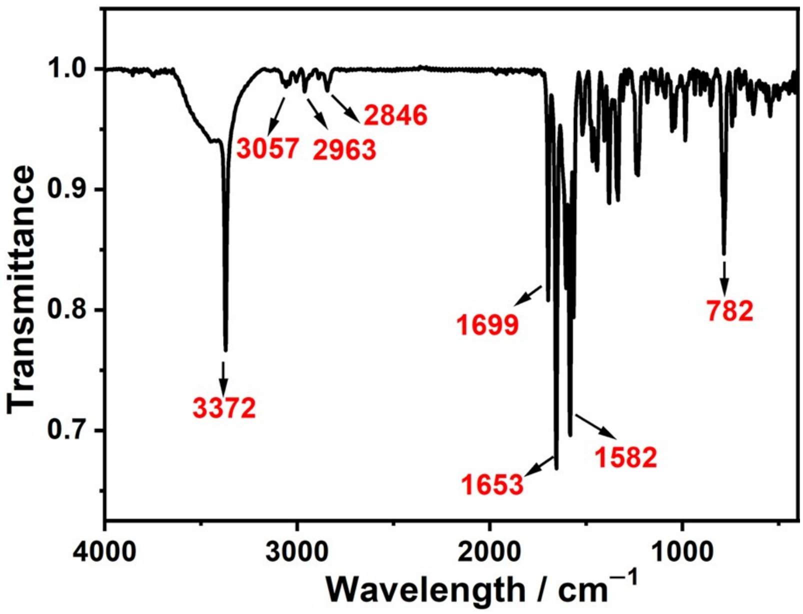

Figure S5 High-resolution IR spectrum of **TL**.

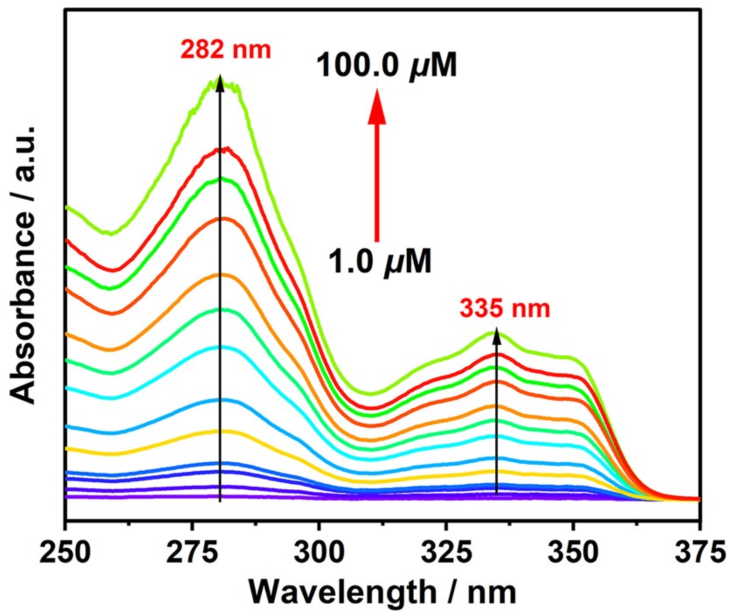

Figure S6 Concentration (form 1.0 μM to 100.0 μM) dependent UV-Vis spectra of **TL** in $CHCl_3$-CH_3CN (7:3, *V/V*) solution.

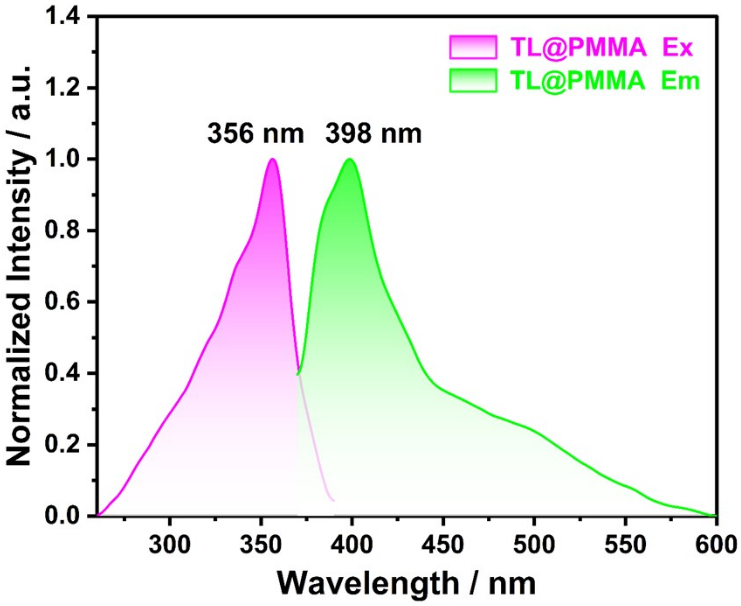

Figure S7 Fluorescence excitation and emission spectra of **TL@PMMA** at 25 °C, respectively.

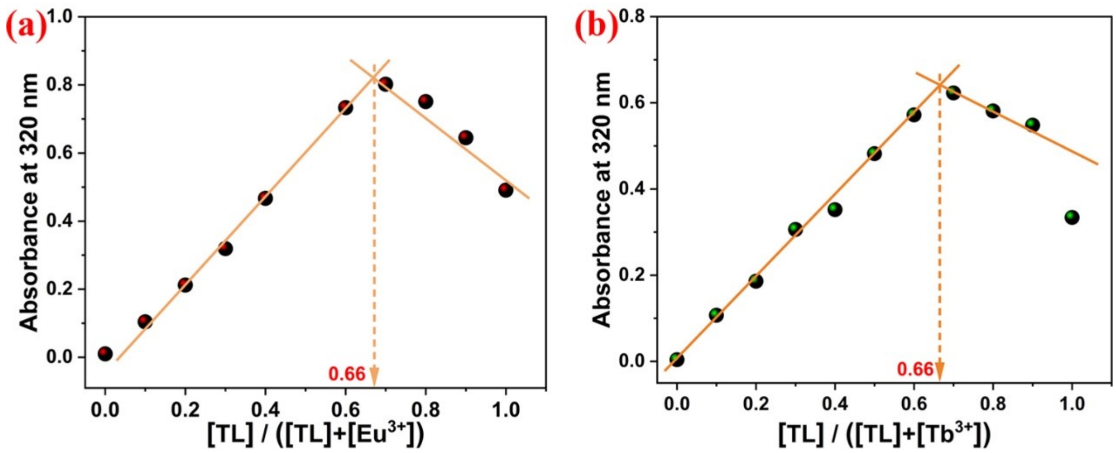

Figure S8 Job's plot of **TL** with Eu^{3+}/Tb^{3+} ([**TL** + Eu^{3+}/Tb^{3+}] = 20 μM) in $CHCl_3$-CH_3CN (7:3, *V/V*) solution shows 2:1 stoichiometry.

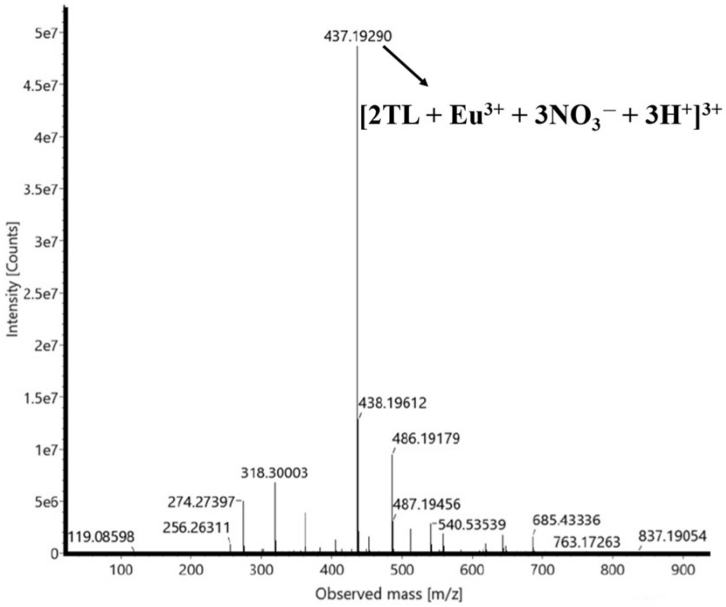

Figure S9 ESI-MS spectrum of **TL-Eu**, Calcd. For $C_{60}H_{49}N_{13}O_{13}Eu$ [2**TL** + Eu^{3+} + $3NO_3^-$ + $3H^+$]$^{3+}$: 437.4262, Found: 437.1929.

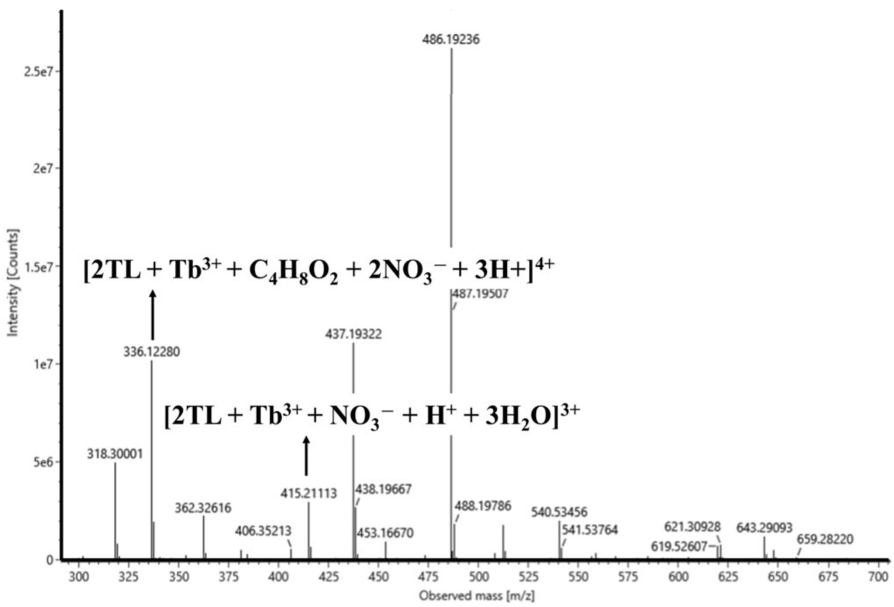

Figure S10 ESI-MS spectrum of **TL-Tb**, Calcd. For $C_{64}H_{57}N_{12}O_{12}Tb$ [2**TL** + Tb^{3+} + $C_4H_8O_2$ + $2NO_3^-$ + $3H^+$]$^{4+}$: 336.0868, Found: 336.1228; Calcd. For $C_{60}H_{53}N_{11}O_{10}Tb$ [2**TL** + Tb^{3+} + NO_3^- + H^+ + $3H_2O$]$^{3+}$: 415.4410, Found: 415.2111, respectively.

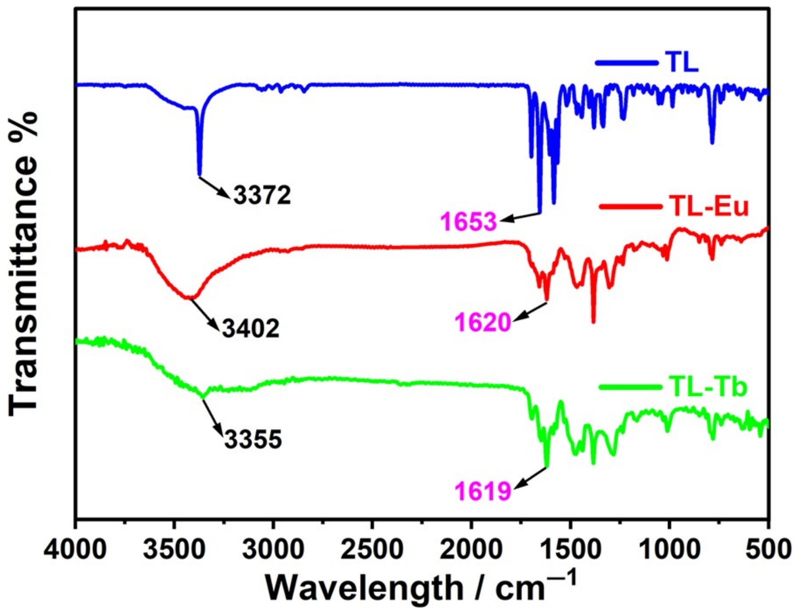

Figure S11 High-resolution IR spectra of **TL**, **TL-Eu** and **TL-Tb**.

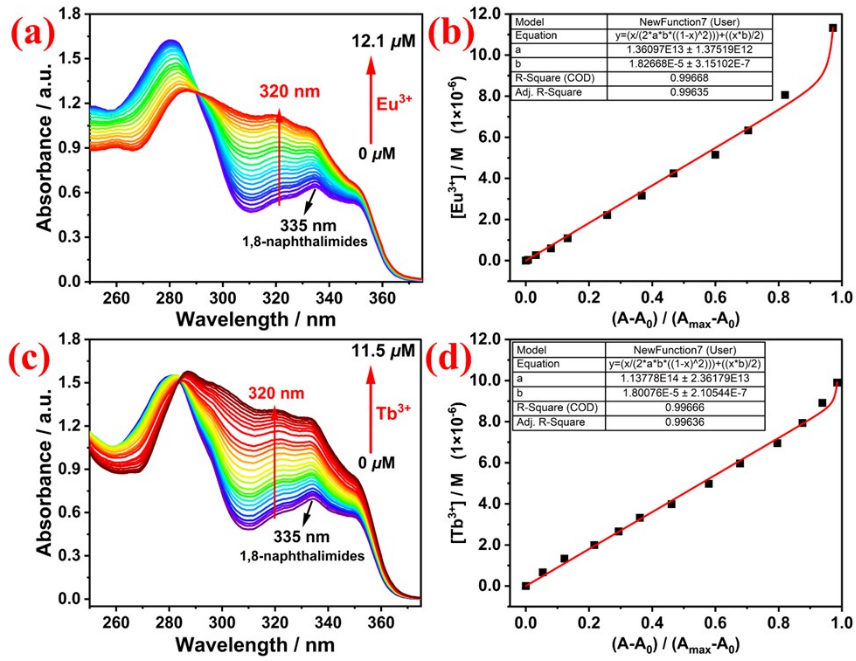

Figure S12 (a,c) UV-Vis consecutive titration of **TL** (40 μM) with Eu^{3+}/Tb^{3+} in $CHCl_3$-CH_3CN (7:3, *V/V*) solution, and (b, d) the result of calculation of K_a by non-linear least square fitting, respectively.

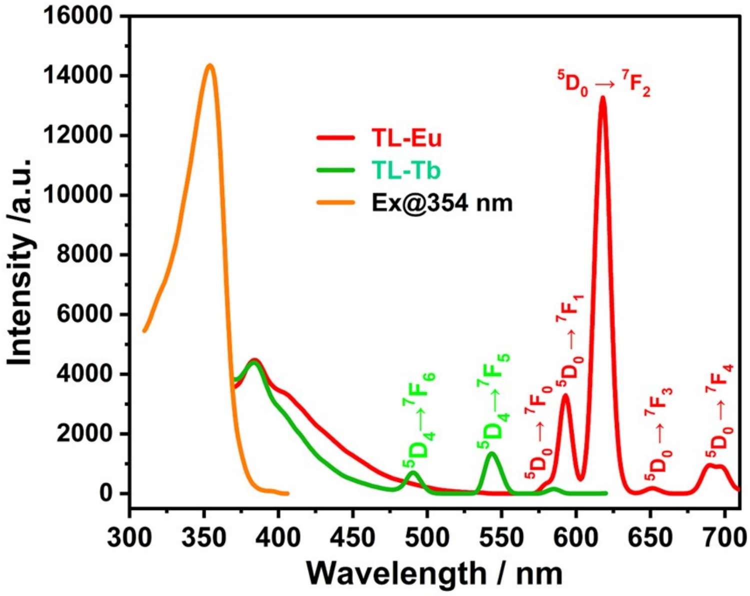

Figure S13 Emission spectra of **TL-Eu/Tb** in $CHCl_3$-CH_3CN (7:3, *V*/*V*) binary solution at 25 °C.

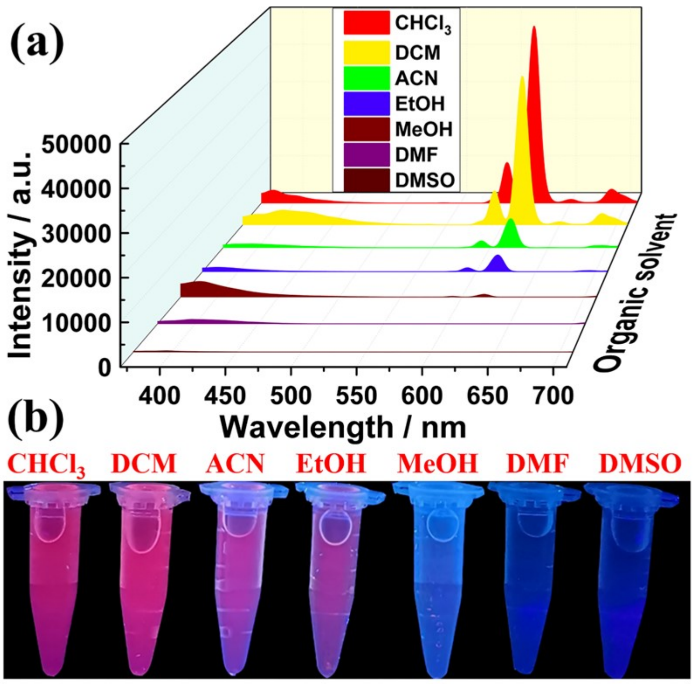

Figure S14 (a) Emission spectra of **TL-Eu** in different solvents upon 354 nm excitation at 25 °C and (b) the corresponding pictures.

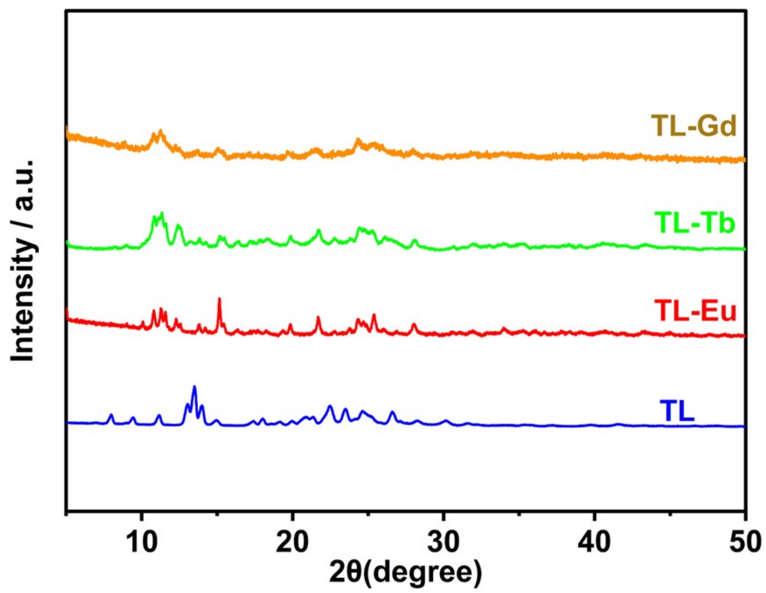

Figure S15 PXRD patterns of **TL**, **TL-Eu**, **TL-Tb** and **TL-Gd**, respectively.

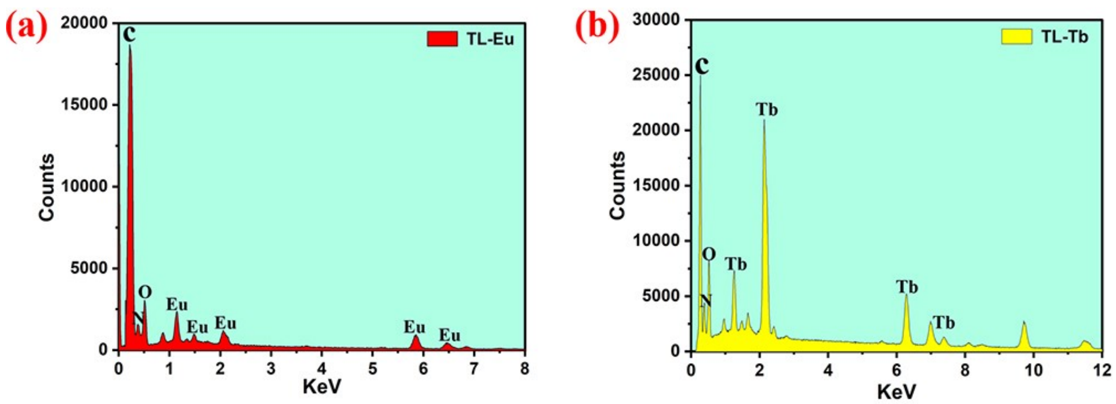

Figure S16 The element content of C, N, O and Eu/Tb elements in EDX energy spectra of **TL-Eu** (a) and **TL-Tb** (b).

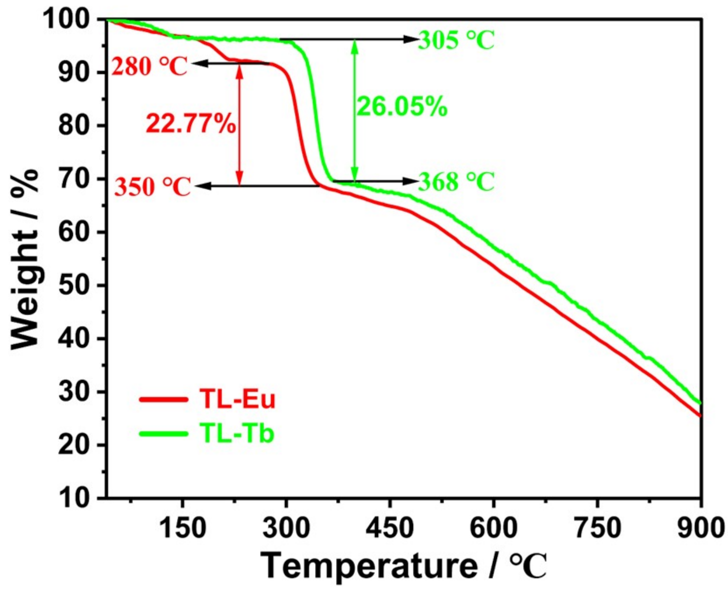

Figure S17 TGA curve of **TL-Eu/Tb** from room temperature to 900 °C.

To investigate the thermal stability of **TL-Eu/Tb**, thermogravimetric analysis was implemented under flowing nitrogen (100 mL·min^{-1}). Solid samples (10 mg) were put placed in an alumina crucible, ramped to 900 °C at a rate of 10 °C min^{-1}, and kept at that temperature for 30 min. It is found that the **TL-Eu/Tb** in solid was not decomposed until 280 °C. These observations indicate that emissive materials have good structural and thermal stability.

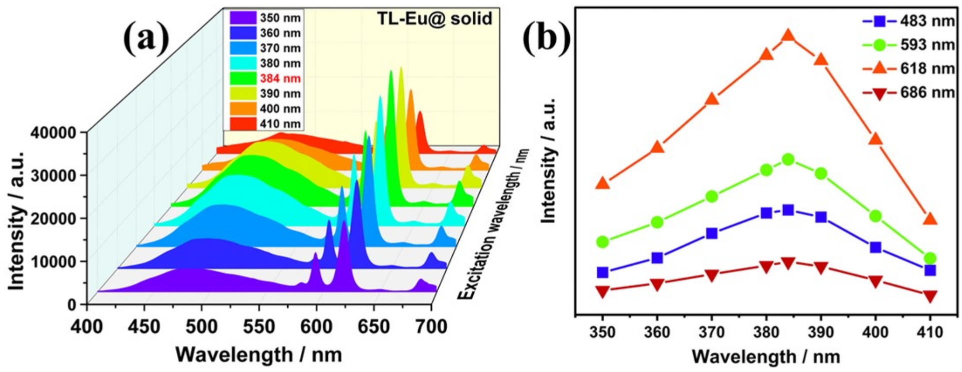

Figure S18 Fluorescence spectra of solid-state **TL-Eu** at different excitation wavelengths (ranging 350-410 nm) at room temperature.

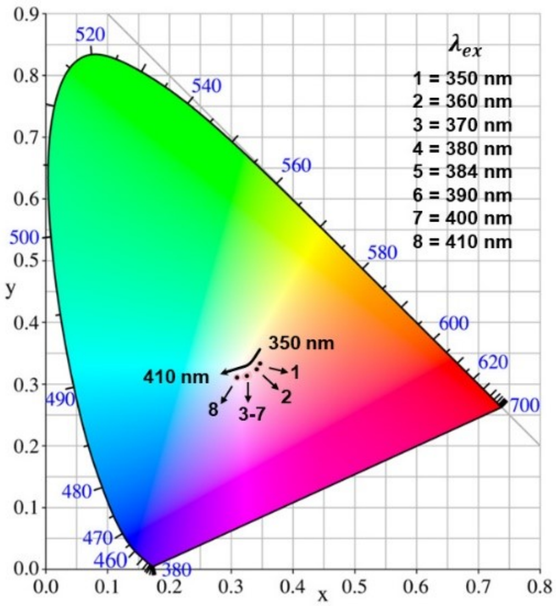

Figure S19 Chromaticity coordinates of **TL-Eu** at different excitation (ranging 350-410 nm).

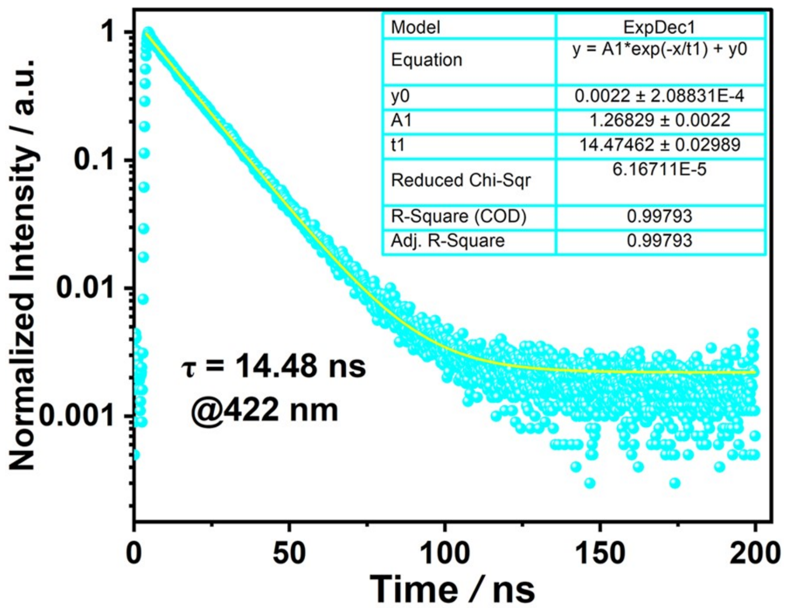

Figure S20 The absolute fluorescence lifetime of solid-state **TL** at 422 nm (λ_{ex} = 355 nm).

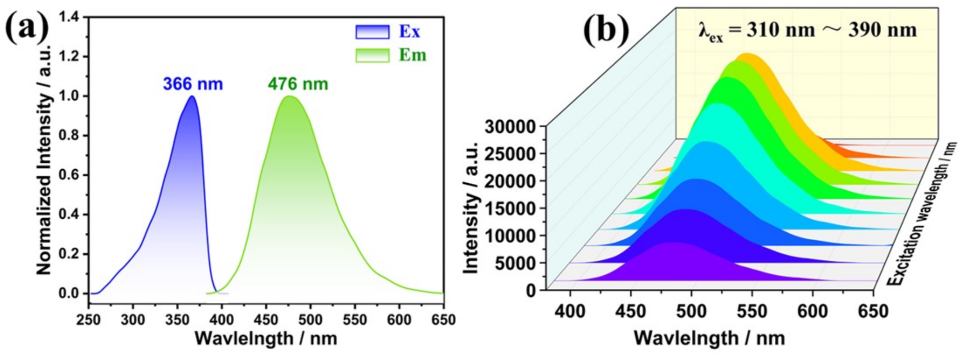

Figure S21 (a) Fluorescence excitation and emission spectra and (b) fluorescence spectra at different excitation wavelengths (ranging 310-390 nm) of solid-state **TL-Tb** at room temperature.

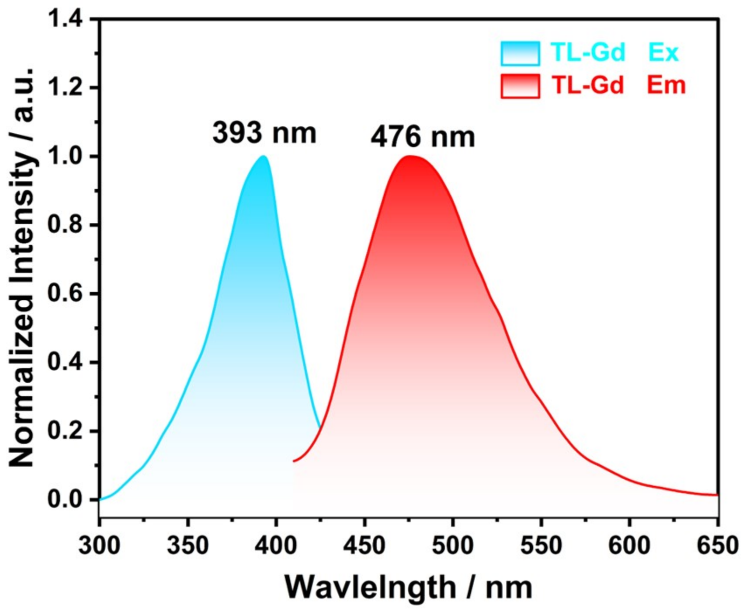

Figure S22 Fluorescence excitation and emission spectra of solid-state **TL-Gd** at 25 °C.

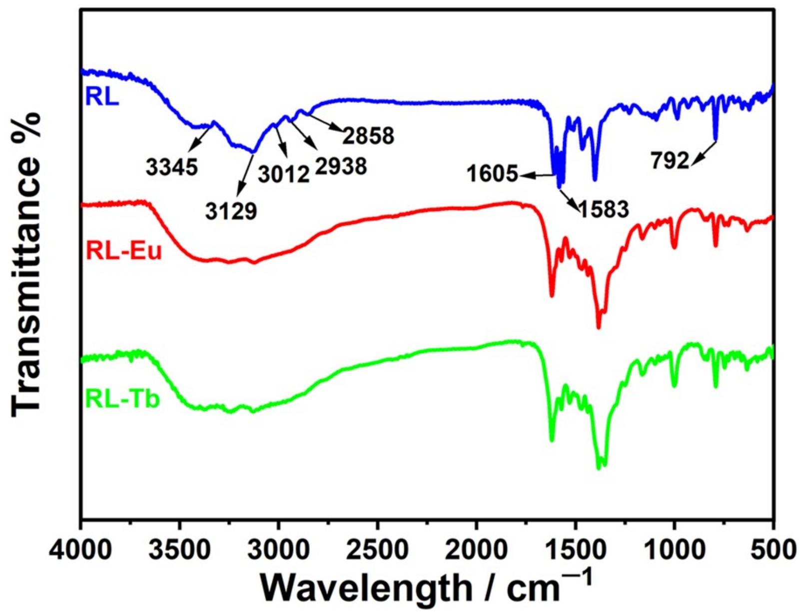

Figure S23 High-resolution IR spectra of **RL**, **RL-Eu** and **RL-Tb**.

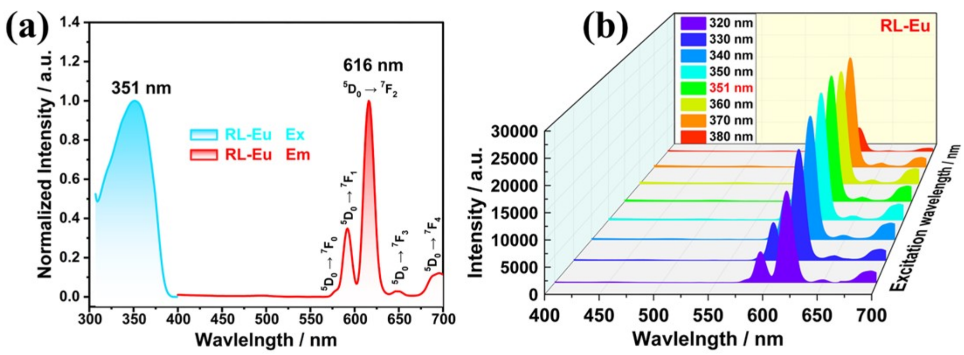

Figure S24 (a) Fluorescence excitation and emission spectra of **RL-Eu** and (b) fluorescence spectra of **RL-Eu** at different excitation wavelengths (ranging 320-380 nm) at room temperature in solid-state.

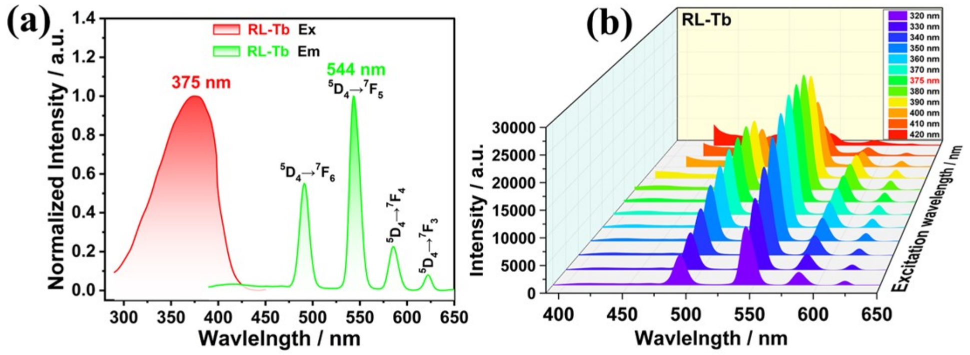

Figure S25 (a) Fluorescence excitation and emission spectra of **RL-Tb** and (b) fluorescence spectra of **RL-Tb** at different excitation wavelengths (ranging 320-420 nm) at room temperature in solid state.

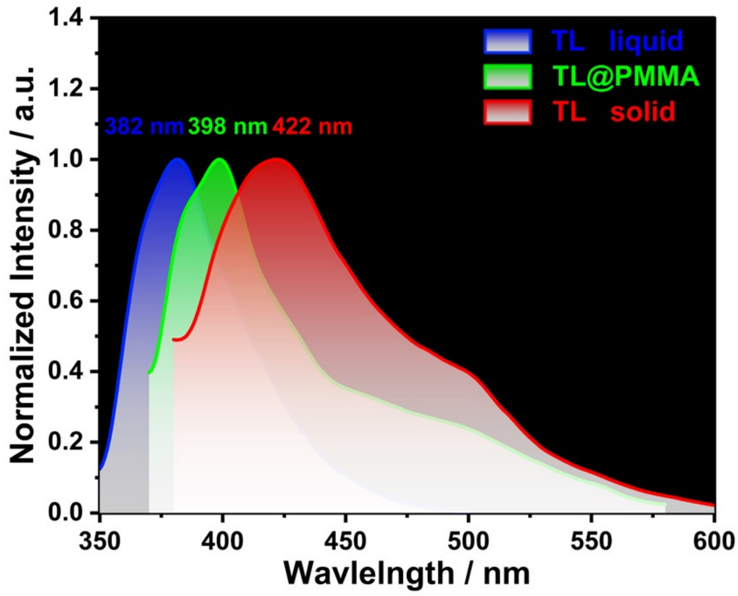

Figure S26 Fluorescence spectra of **TL** in solution (blue line), doped state (0.5% **TL@PMMA,** green line) and solid-state (red line) at room temperature.

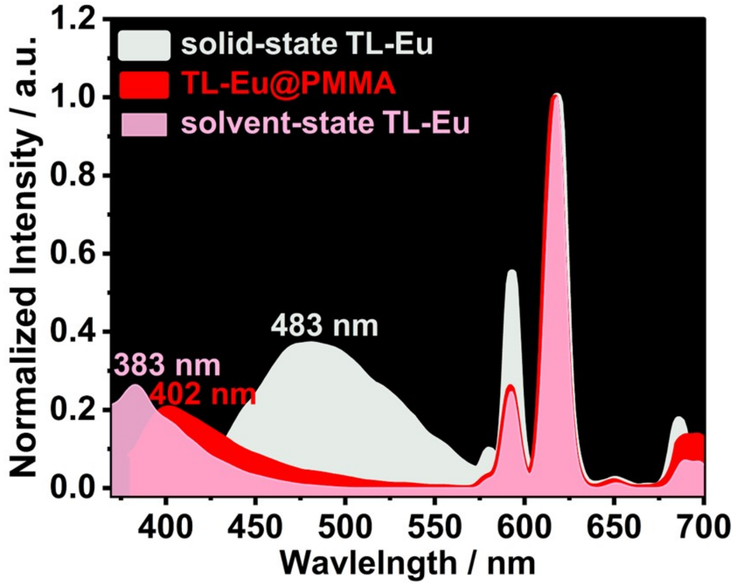

Figure S27 Fluorescence spectra of **TL-Eu** in solution (pink line), doped state (0.5% **TL-Eu@PMMA,** red line) and solid-state (white line) at room temperature.

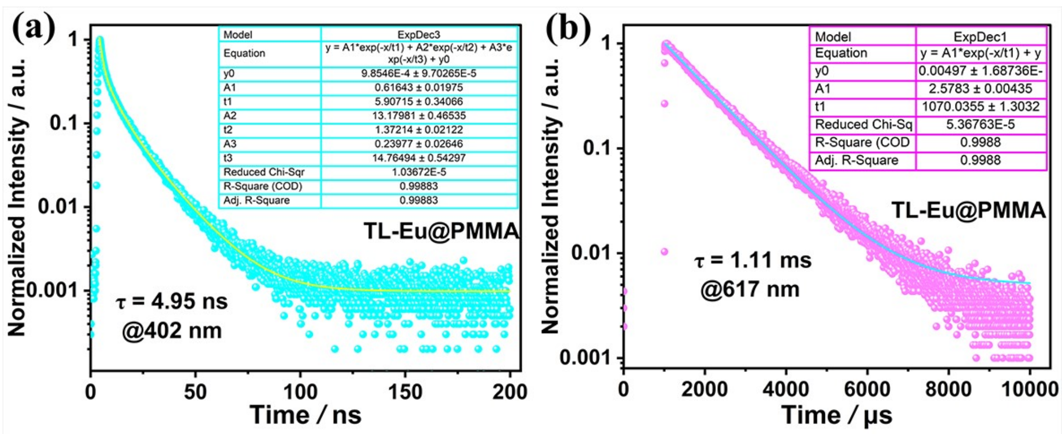

Figure S28 (a) **TL**-centered (402 nm) and (b) Eu^{3+}-centered (617 nm) fluorescence lifetimes of **TL-Eu@PMMA** film (λ_{ex} = 350 nm).

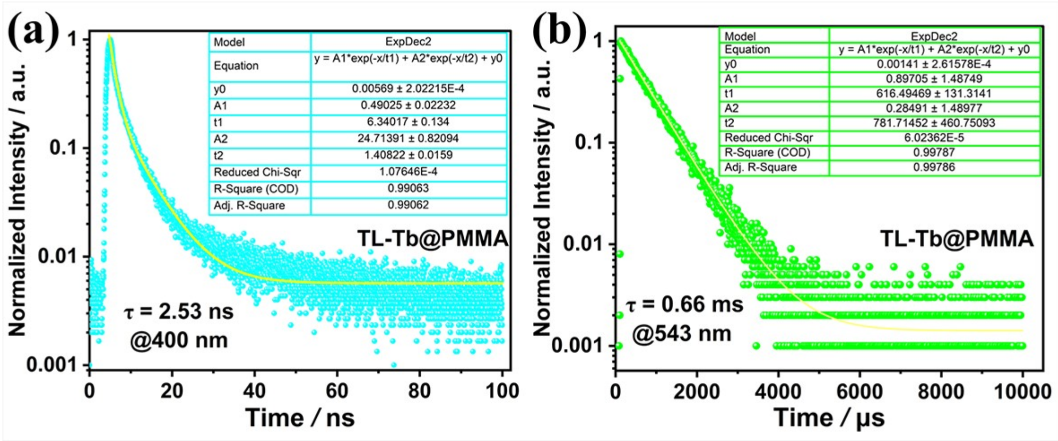

Figure S29 (a) **TL**-centered (400 nm) and (b) Tb^{3+}-centered (543 nm) fluorescence lifetimes of **TL-Tb@PMMA** film (λ_{ex} = 350 nm).

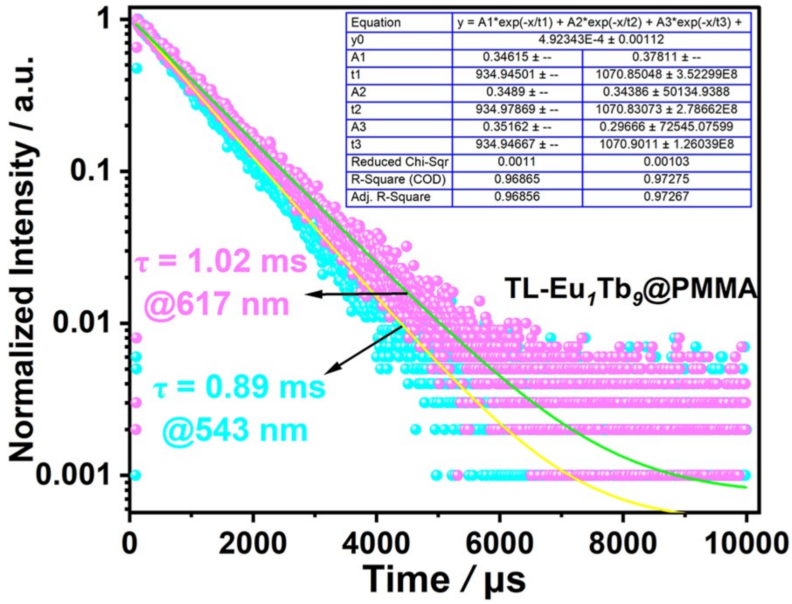

Figure S30 Eu^{3+}/Tb^{3+}-centered (617 nm/543 nm) fluorescence lifetimes of **TL-Eu$_1$Tb$_9$@PMMA** (λ_{ex} = 361 nm).

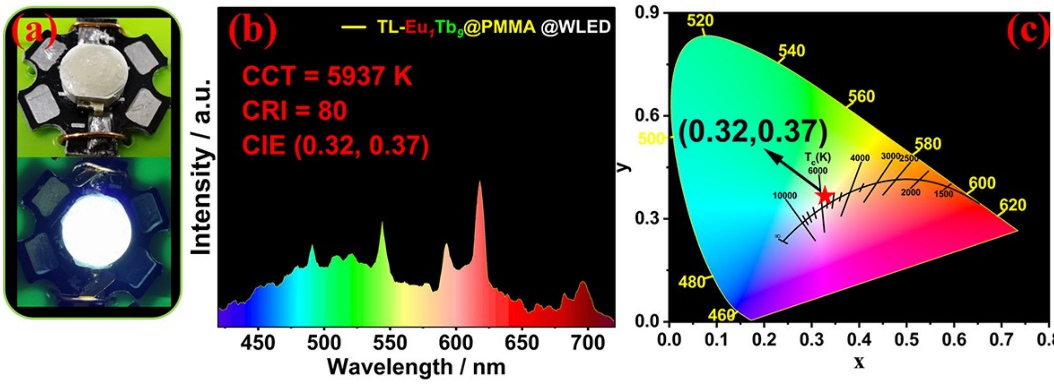

Figure S31. (a) Photos of 365 nm LED with coated **TL-Eu$_1$Tb$_9$@PMMA** when LED is off and on, (b, c) the corresponding emission spectra and CIE coordinate of WLED, respectively.

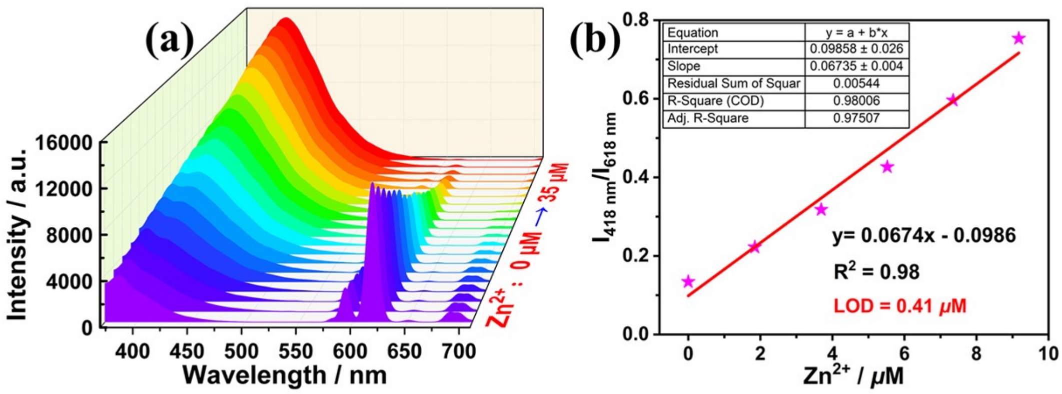

Figure S32 (a) Fluorescence consecutive titration of **TL-Eu** (50 μM) with Zn^{2+} in $CHCl_3$-CH_3CN (7:3, *V/V*) solution, and (b) the calculation of LOD.

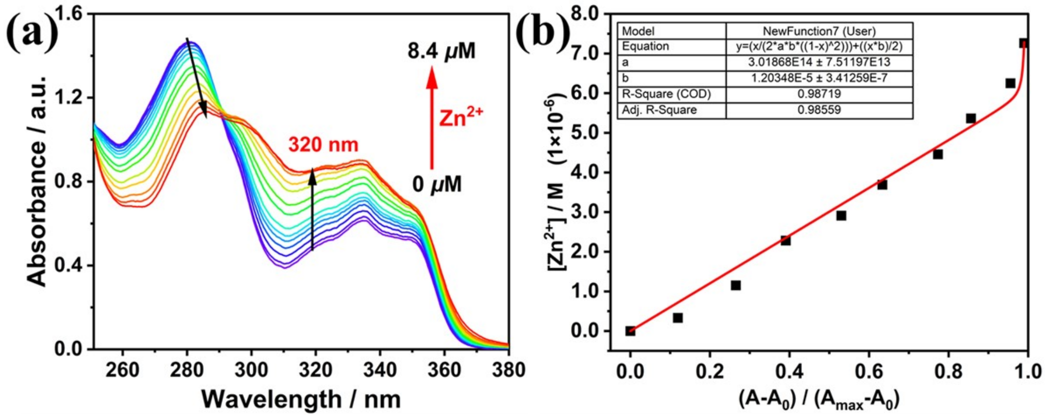

Figure S33 (a) UV-Vis consecutive titration of **TL** (40 μM) with Zn^{2+} in $CHCl_3$-CH_3CN (7:3, *V/V*) solution, and (b) the result of calculation of K_a.

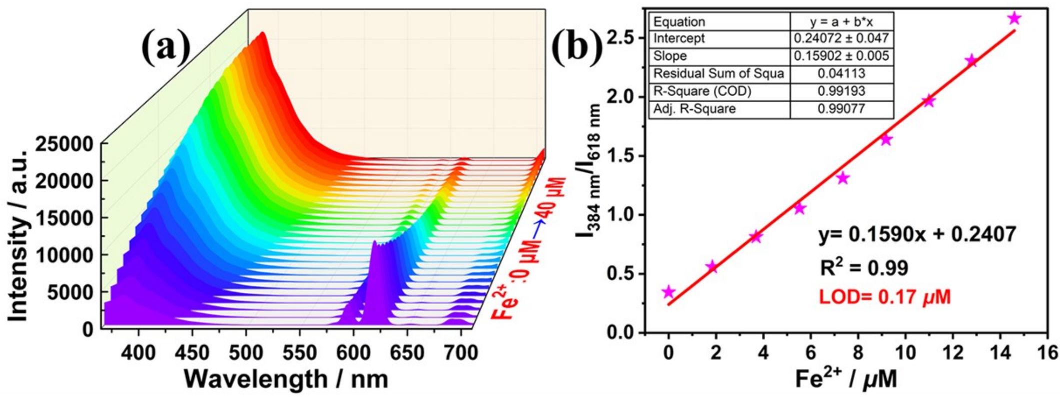

Figure S34 (a) Fluorescence consecutive titration of **TL-Eu** (50 μM) with Fe^{2+} in $CHCl_3$-CH_3CN (7:3, *V/V*) solution, and (b) the calculation of LOD.

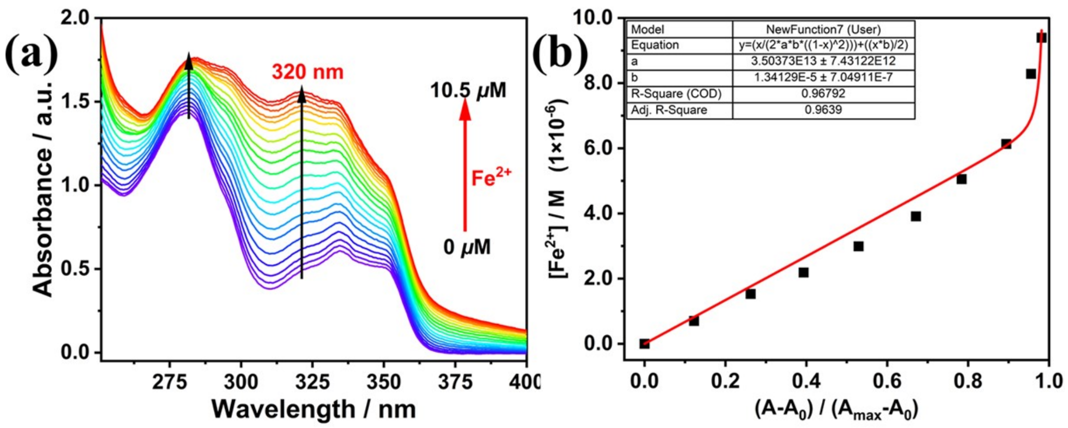

Figure S35 (a) UV-Vis consecutive titration of **TL** (40 μM) with Fe^{2+} in $CHCl_3$-CH_3CN (7:3, *V/V*) solution, and (b) the result of calculation of K_a by non-linear least square fitting, respectively.

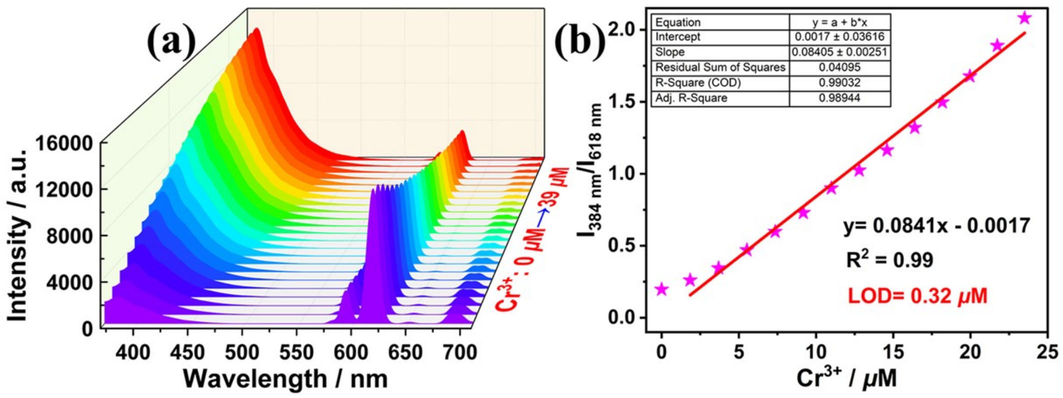

Figure S36 (a) Fluorescence consecutive titration of **TL-Eu** (50 μM) with Cr^{3+} in $CHCl_3$-CH_3CN (7:3, *V/V*) solution, and (b) the calculation of LOD.

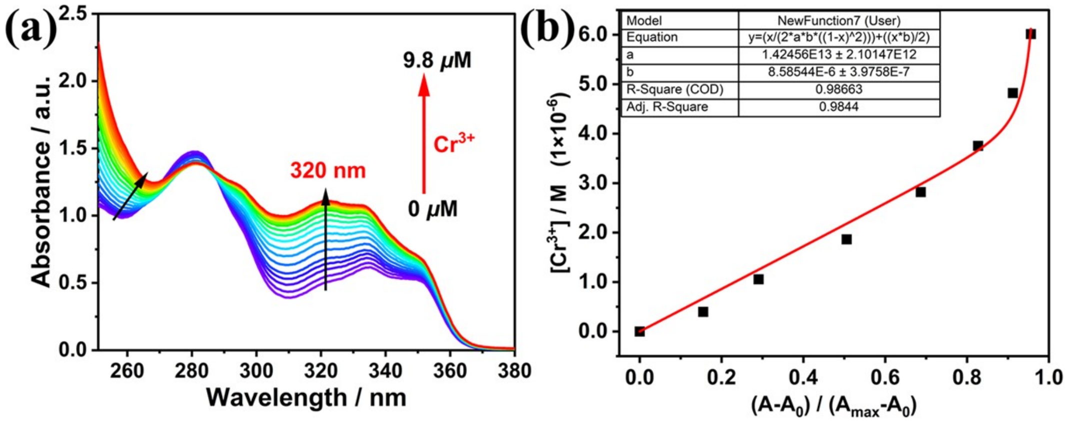

Figure S37 (a) UV-Vis consecutive titration of **TL** (40 μM) with Cr^{3+} in $CHCl_3$-CH_3CN (7:3, *V/V*) solution, and (b) the result of calculation of K_a by non-linear least square fitting, respectively.

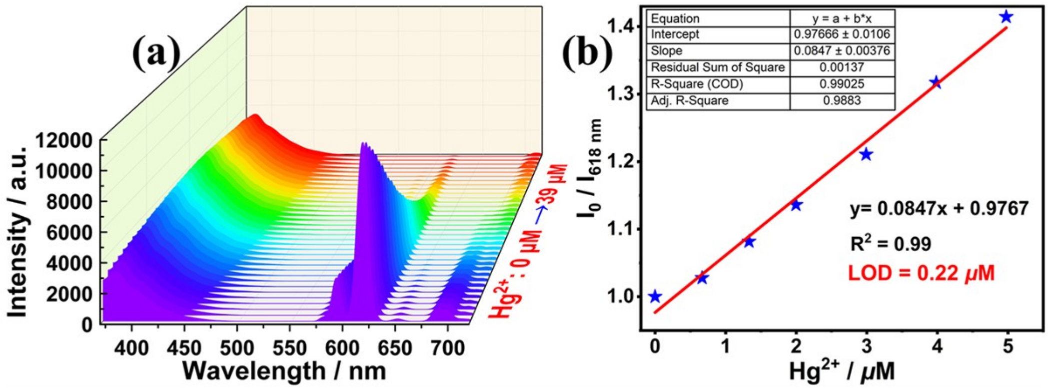

Figure S38 (a) Fluorescence consecutive titration of **TL-Eu** (50 μM) with Hg^{2+} in $CHCl_3$-CH_3CN (7:3, *V/V*) solution, and (b) the calculation of LOD.

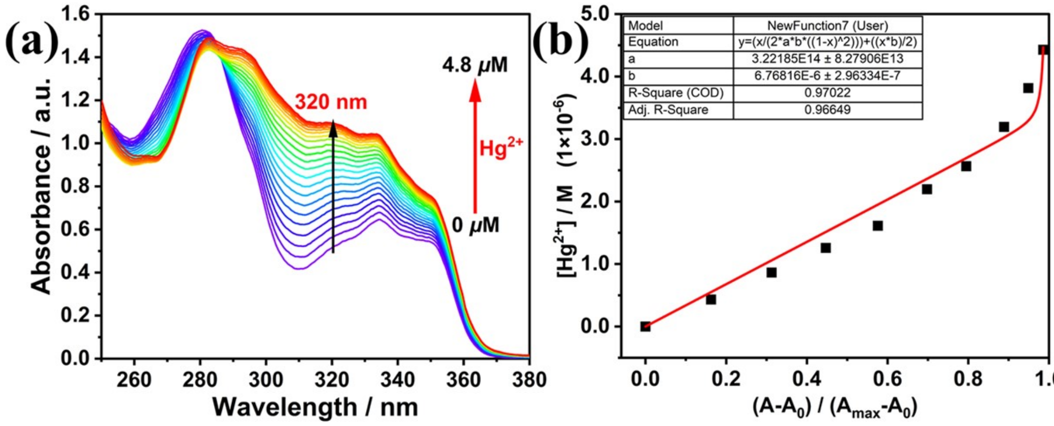

Figure S39 (a) UV-Vis consecutive titration of **TL** (40 μM) with Hg^{2+} in $CHCl_3$-CH_3CN (7:3, *V/V*) solution, and (b) the result of calculation of K_a by non-linear least square fitting, respectively.

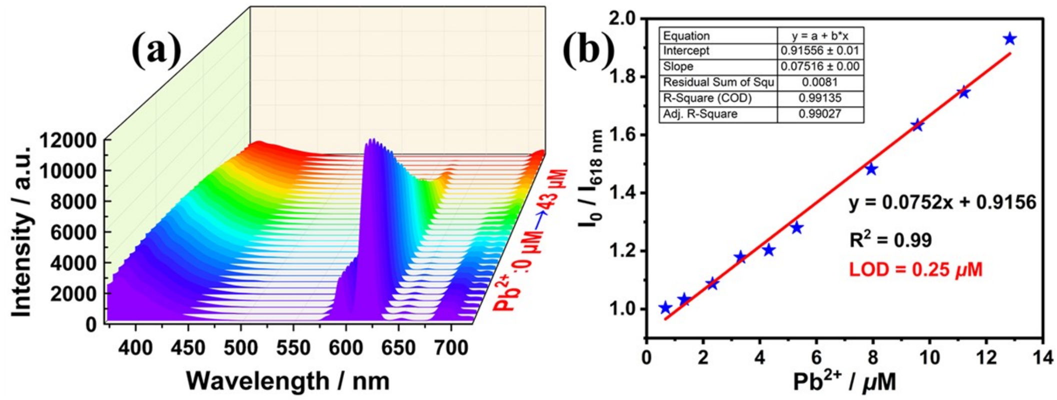

Figure S40 (a) Fluorescence consecutive titration of **TL-Eu** (50 μM) with Pb^{2+} in $CHCl_3$-CH_3CN (7:3, *V/V*) solution, and (b) the calculation of LOD.

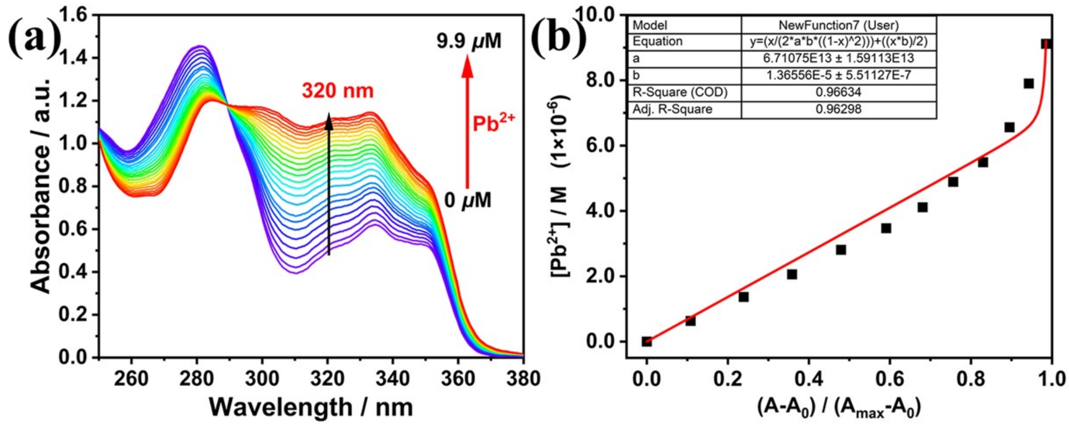

Figure S41 (a) UV-Vis consecutive titration of **TL** (40 μM) with Pb^{2+} in $CHCl_3$-CH_3CN (7:3, *V/V*) solution, and (b) the result of calculation of K_a by non-linear least square fitting, respectively.

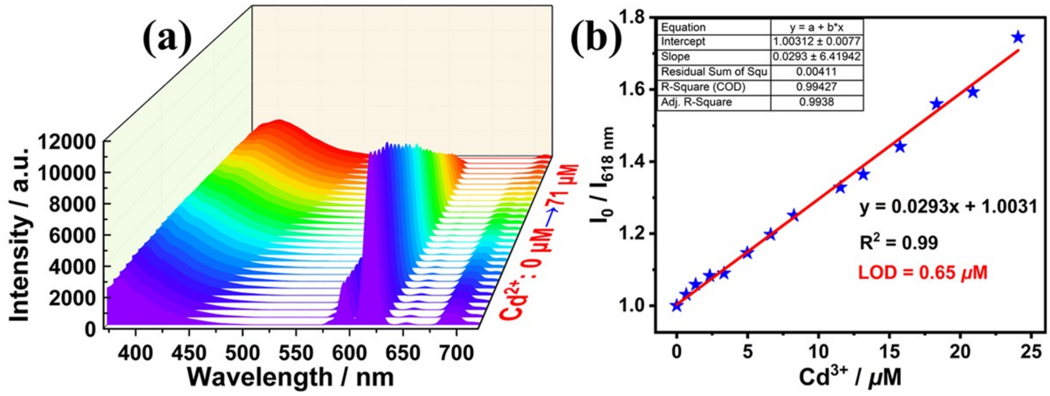

Figure S42 (a) Fluorescence consecutive titration of **TL-Eu** (50 μM) with Cd^{2+} in $CHCl_3$-CH_3CN (7:3, *V/V*) solution, and (b) the calculation of LOD.

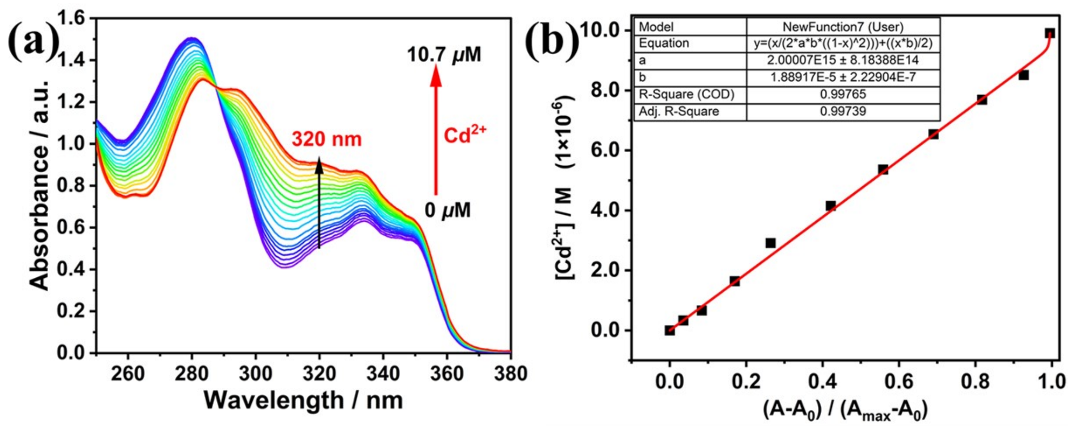

Figure S43 (a) UV-Vis consecutive titration of **TL** (40 μM) with Cd^{2+} in $CHCl_3$-CH_3CN (7:3, *V/V*) solution, and (b) the result of calculation of K_a by non-linear least square fitting, respectively.

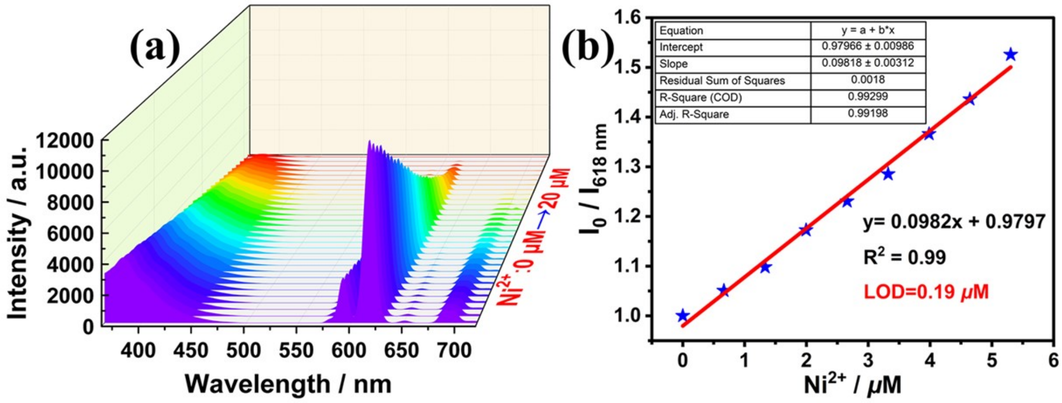

Figure S44 (a) Fluorescence consecutive titration of **TL-Eu** (50 μM) with Ni^{2+} in $CHCl_3$-CH_3CN (7:3, *V/V*) solution, and (b) the calculation of LOD.

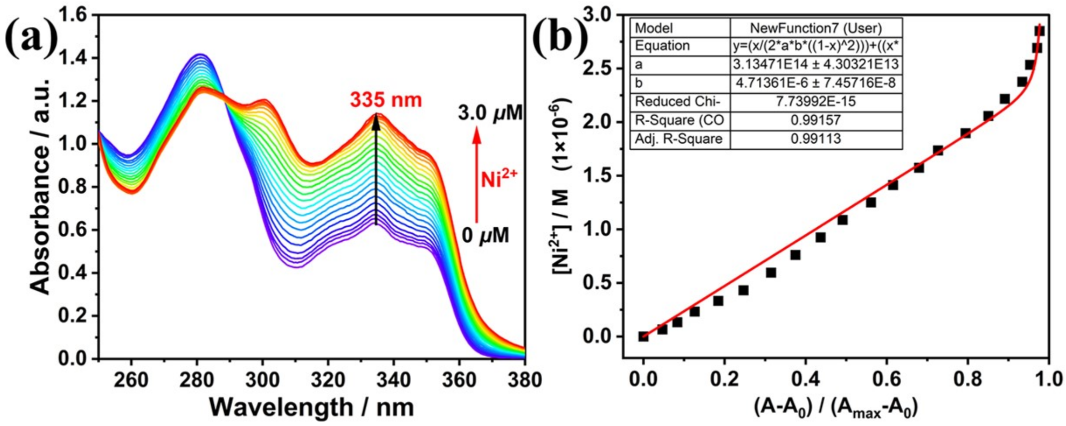

Figure S45 (a) UV-Vis consecutive titration of **TL** (40 μM) with Ni^{2+} in $CHCl_3$-CH_3CN (7:3, *V/V*) solution, and (b) the result of calculation of K_a by non-linear least square fitting, respectively.

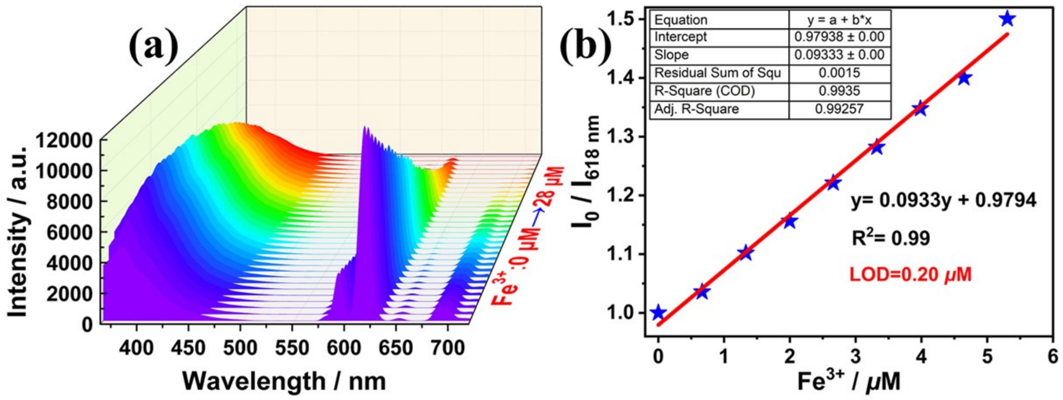

Figure S46 (a) Fluorescence consecutive titration of **TL-Eu** (50 μM) with Fe^{3+} in $CHCl_3$-CH_3CN (7:3, *V/V*) solution, and (b) the calculation of LOD.

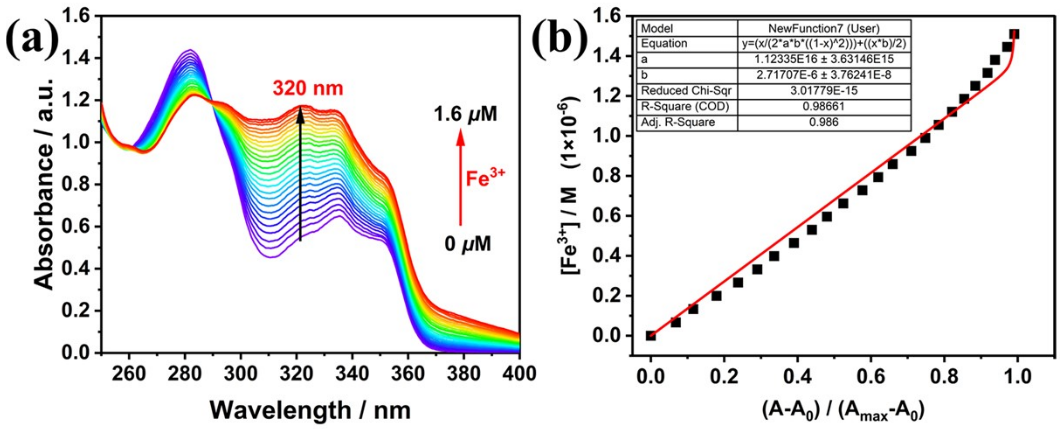

Figure S47 (a) UV-Vis consecutive titration of **TL** (40 μM) with Fe^{3+} in $CHCl_3$-CH_3CN (7:3, *V/V*) solution, and (b) the result of calculation of K_a by non-linear least square fitting, respectively.

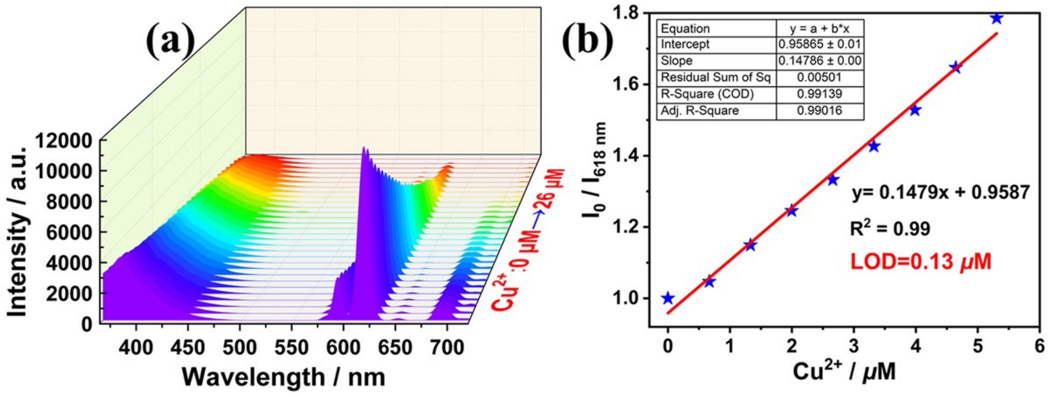

Figure S48 (a) Fluorescence consecutive titration of **TL-Eu** (50 μM) with Cu^{2+} in $CHCl_3$-CH_3CN (7:3, *V/V*) solution, and (b) the calculation of LOD.

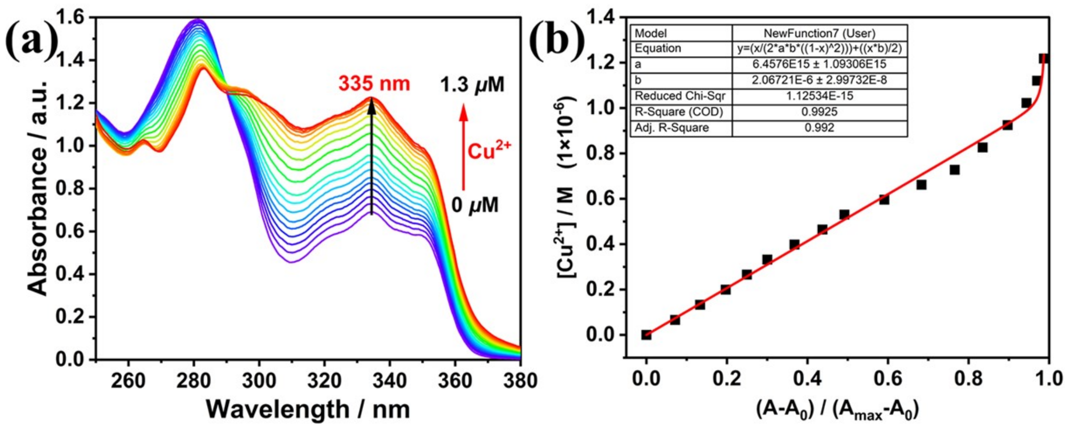

Figure S49 (a) UV-Vis consecutive titration of **TL** (40 μM) with Cu^{2+} in $CHCl_3$-CH_3CN (7:3, *V/V*) solution, and (b) the result of calculation of K_a by non-linear least square fitting, respectively.

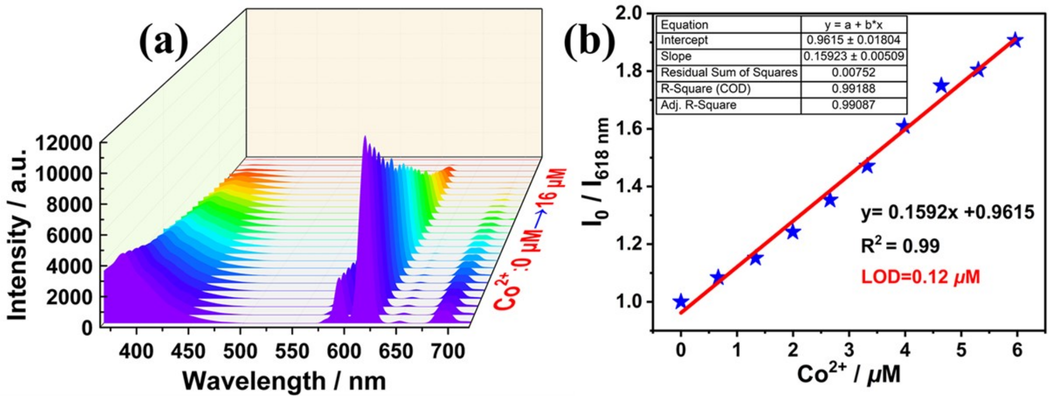

Figure S50 (a) Fluorescence consecutive titration of **TL-Eu** (50 μM) with Co^{2+} in $CHCl_3$-CH_3CN (7:3, *V/V*) solution, and (b) the calculation of LOD.

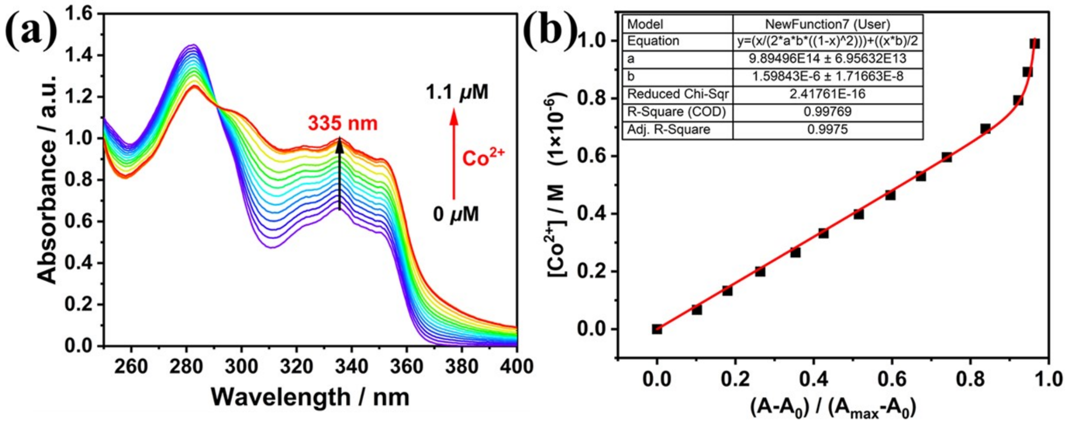

Figure S51 (a) UV-Vis consecutive titration of **TL** (40 μM) with Co^{2+} in $CHCl_3$-CH_3CN (7:3, *V/V*) solution, and (b) the result of calculation of K_a by non-linear least square fitting, respectively.

The addition of Zn^{2+}, Fe^{2+} and Cr^{3+} induced the turning off of Eu-centered emission at 618 nm, resulting in the blue emission only (Zn^{2+}-induced redshift also can be found). Correspondingly, their solution color changed from pink to blue. Besides, Co^{2+}, Fe^{3+}, Hg^{2+}, Cu^{2+}, Pb^{2+}, Ni^{2+} and Cd^{2+} extremely triggered the quenching of red and blue emissions to a different extent. Whereas, other cations (Mg^{2+}, Ca^{2+}, K^+ and Na^+) brought negligible spectral responses. Thus, the visual sensing of **TL-Eu** solution toward multiple heavy metal ions was well conducted, which was further demonstrated with the help of detailed spectroscopy titration experiments, from Fig. S32 to S51. The association constants (K_a) were obtained from absorption spectral titration, while the LOD were received based on emission spectral titration, respectively. The Benesi-Hildebrand plots gave the corresponding stoichiometry (2:1) between ligand and heavy metal ions (**TL-M**). Table S6 represents these physical parameters including the CIE coordinates at the endpoint of the titration, showing the K_a values of **TL**-M are more than that of **TL-Eu** (1.36×10^{13} M^{-1}). Therefore, we can reasonably confirm that the **TL-Eu** complex will be dissociated and heavy metal complexes are formed, due to the competition coordination, leading to the quenching of red emission. By the way, the LODs of these cations were found to be in the range of 0.12-0.65 μM for emission spectral titration experiments, respectively.

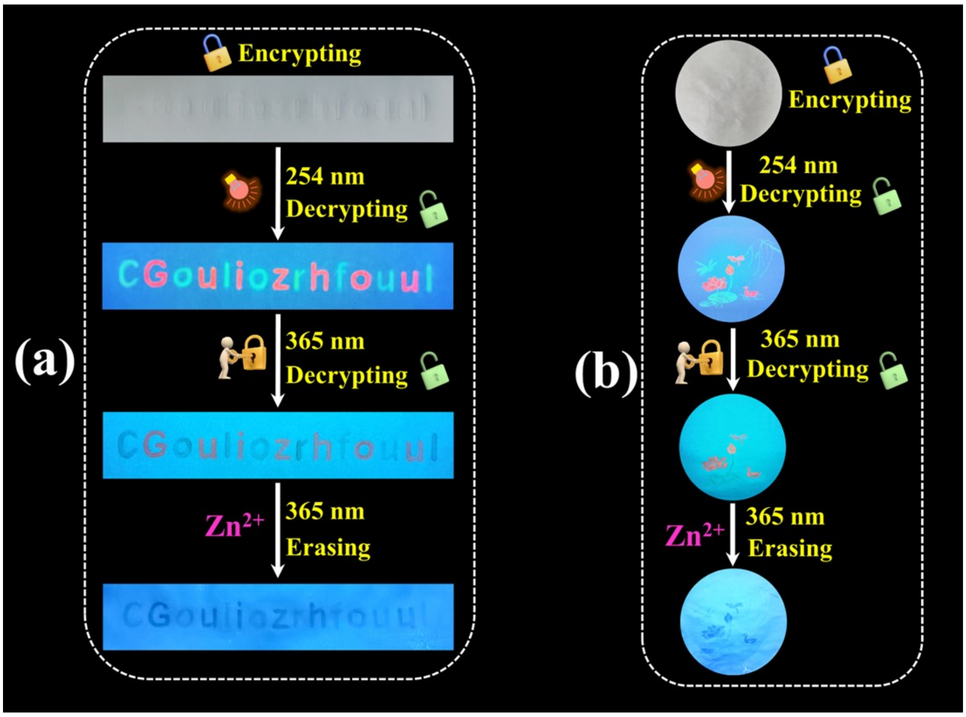

Figure S52 (a) The words "Colorful Guizhou" are encryption by scrambled letters, and (b) The pattern of colorful painting. Notes: the (a), (b) patterns are invisible in daylight, visible at 254 nm, while the right information is extracted under 365 nm irradiation, and eliminated when they were immersed in Zn^{2+} solution (20 μM).

3. *Supporting tables*

Table S1. The excitation-dependent CIE (x,y) coordinates, CCT and CRI values of **TL-Eu**, respectively.

λ_{ex}(nm)	X	Y	CCT(K)	CRI
350	0.347	0.333	4753	64.5
354	0.337	0.331	5261	64.3
356	0.337	0.330	5299	63.9
358	0.336	0.329	5335	63.1
360	0.335	0.327	5388	62.4
370	0.321	0.307	5714	58.5
380	0.341	0.331	6023	58.4
384	0.327	0.313	5785	57.5
390	0.325	0.313	5924	58.5
400	0.325	0.313	5945	61.9
410	0.309	0.311	6958	73.9

Table S2. The emission parameters of single Eu^{3+}-doped WLE materials.

constitute	λ_{ex} (nm)	CIE	QY (%)	τ (ms)	CCT(K)	CRI	Ref.
TL-Eu	**354-360**	**(0.34, 0.33)** [a]	**6.4**	**0.56**	**5261-5388**	**62-64**	**This work**
10%Eu-doped SMOF-1	394	(0.30, 0.34) [a]	4.3		3606-6839	63-93	[S5]
$[Eu_2L_4(HFAC)](O_2CCF_3)\cdot 2H_2O$	368	(0.34, 0.33) [b]	- [e]	0.13	-	-	[S6]
$\{[Eu(L^2)_3(H_2O)]\cdot H_2O\}_n$	320	(0.34, 0.31) [a]	11.9	0.27	-	-	[S7]
$Eu(TTA)_3$−Phen−Fl−TPA−DPA	380	(0.34, 0.33) [b]	15.3	-	5152	-	[S8]
$[EuL(NO_3)_3]_n\cdot 2C_4H_8O_2$ $[EuL(NO_3)_3]_n\cdot 2C_4H_8O_2$@PMMA	285 345 296	(0.33, 0.35) [a] (0.34, 0.32) [a] (0.33, 0.31) [c]	-	-	-	-	[S9]
AIE/Eu^{3+}-Doped WLE Ion Gel	254	(0.31, 0.32) [d]	-	-	-	-	[S10]
$[Eu(tta)_3L_1]$ **(1)** $[Eu(tta)_3L_2]$ **(3)**	343 344	(0.31, 0.33) [b] (0.33, 0.31) [b]	2.6 1.8	0.65 0.65	-	-	[S11]
EuL EuL@PMMA	334 275	(0.33, 0.32) [a] (0.33,0.33) [c]	-	-	-	-	[S12]
$Eu(TTA)_3$-TPA-DPA-mCF_3	345	(0.35,0.34) [a]	-	-	4645	-	[S13]
Eu^{3+}@PY-DPA-CB[8]	302	(0.34,0.31) [b]	-	-	-	-	[S14]
$Eu(1)_3$	275 250 (270-272)	(0.32,0.29) [a] (0.33,0.28) [b] (0.33, 0.28) [c]	-	-	-	-	[S15]

[a] Solid state; [b] Solvent state; [c] film; [d] gel; [e] No available date.

Table S3. Relative intensities (contributions) of the ligand-centered bands at 483 nm and Eu(III)-centered $^5D_0 \rightarrow ^7F_J$ (J = 1-4) transitions normalized to the $^5D_0 \rightarrow ^7F_2$ band in the emission spectra of solid-state **TL-Eu** under excitation at 354-360 nm.

	354 nm	356 nm	358 nm	360 nm
483 nm	16.10%	16.20%	16.29%	16.41%
580 nm	5.59%	5.59%	5.50%	5.34%
593 nm	24.32%	24.24%	24.27%	24.14%
618 nm	44.91%	44.87%	44.84%	45.01%
650 nm	1.42%	1.45%	1.45%	1.44%
686 nm	7.65%	7.65%	7.66%	7.66%

Table S4. The emission parameters (CIE, CCT and CRI) of WLED in this work and previously reported ones.

constitute	CIE	CCT(K)	CRI	Ref.
TL-Eu	**(0.32, 0.34)**	**6192**	**94**	**This work**
TL-Eu_1Tb_9@PMMA	**(0.32, 0.37)**	**5937**	**80**	**This work**
$Eu_{0.5}Tb_{0.5}$-Ln-nanopaper@FB	(0.34, 0.36)	5536	86	[S16]
$Eu_{0.045}Tb_{0.955}$CPOMBA	(0.33, 0.34)	5733	73	[S17]
CGB-a:$(MOF\text{-}Eu)_{3.5}$	(0.42, 0.38)	3020	92	[S18]
$Eu(DBM)_3L\text{-}pCH_3$	(0.36, 0.35)	4234	75	[S19]
CMCh-Eu^{3+}/Tb^{3+}(3/7)	(0.36, 0.40)	4705	88.6	[S20]
Tb/Eu@bio-MOF-1(0.06/0.5)	(0.36, 0.40)	4725	86.2	[S21]
$Eu(TTA)_3$−Phen−Fl−TPA−DPA	(0.34, 0.33)	5152	-[a]	[S8]
$Eu_{0.03}Tb_{0.03}La_{0.94}$-MOF	(0.31, 0.32)	6516	90	[S22]
Poly-Eu-Tb-CNFs	(0.39, 0.32)	3347	84	[S23]
$Eu(TTA)_3$-TPA-DPA-mCF_3	(0.35, 0.34)	4645	86	[S24]
Eu-**3**	(0.37, 0.34)	3955	83	[S25]
poly-$Eu(TTA)_3$ **(2)**	(0.32, 0.34)	6201	86.1	[S26]
CQDs-N:Eu^{3+}@MOF-Gd:Eu^{3+}/Tb^{3+}	(0.38, 0.38)	4035	95[b]	[S27]
GGTO:0.6Eu^{3+}+$(Ba,Sr)_2SiO_4$:Eu^{2+}+ BAM:Eu^{2+}	(0.38, 0.41)	4331	91.9	[S28]
$Ca_2Gd_{0.5}Nb_{0.95}W_{0.04}O_6$:0.5$Eu^{3+}$	-[a]	5386	91	[S29]
"G+R+B" WLED	(0.34, 0.31)	5308	81.5	[S30]
$CaLa_4Ti_4O_{15}$:Eu^{3+}, Gd^{3+} + BSS:Eu^{2+} + BAM:Eu^{2+}	(0.35, 0.35)	4761	93.1	[S31]
KSGO:0.08Eu^{3+}+BAM:Eu^{2+} + Sr_2SiO_4:Eu^{2+}	(0.34, 0.33)	4963	84.7	[S32]
$Sr_2SiO_4Eu^{2+}$+$BaMgAl_{10}O_7$：Eu^{2+} + CSO:0.15Eu^{3+},0.03Sm^{3+}	(0.34, 0.35)	5348	81	[S33]
K_2MgGeO_4:Eu^{3+}/$BaMgAl_{10}O_{17}$:Eu^{2+} /$(Sr,Ba)_2SiO_4$:Eu^{2+} = 10/1/3	(0.31, 0.34)	6648	91.7	[S34]

[a)] No available date; [b)] The reported highest CRI value.

Table S5 Excitation wavelength-dependent luminescence lifetimes (τ) and absolute fluorescence quantum efficiencies (QY).

Samples	λ_{ex}(nm)	$\tau_{(L)}$/ns (λ_{em}/nm)	$\tau_{(Ln)}$/ms (λ_{em}/nm)	QY (%)
TL	355	14.48 (422)	–	–
TL-Eu	356	10.39 (483)	0.56 (618)	6.40
TL-Eu@PMMA	350	4.95 (402)	1.11 (617)	5.09
TL-Tb@PMMA	350	2.53 (400)	0.66 (543)	2.33
$TL-Eu_1Tb_9$@PMMA	361	–	Eu: 1.02 (617)	3.98
			Tb: 0.89 (543)	1.52

a) λ_{ex} and λ_{em} represent excitation and emission wavelengths, b) $\tau_{(L)}$ and $\tau_{(Ln)}$ represent ligand and Ln^{3+}-centered lifetimes of corresponding samples.

Table S6 The association constant (K_a), the limit of detection (LOD) for different metal ions, and CIE coordinates of corresponding solutions at the endpoint of the titration.

	K_a/M	**LOD/μM**	**CIE (end)**
Eu^{3+}	1.36×10^{13}	-	-
Tb^{3+}	1.13×10^{14}	-	-
Zn^{2+}	3.02×10^{14}	0.41	(0.16, 0.07)
Fe^{2+}	3.50×10^{13}	0.17	(0.17, 0.04)
Cr^{3+}	1.42×10^{13}	0.32	(0.26, 0.09)
Hg^{2+}	3.22×10^{14}	0.22	(0.16, 0.03)
Pb^{2+}	6.71×10^{13}	0.25	(0.16, 0.02)
Cd^{2+}	2.00×10^{15}	0.65	(0.15, 0.07)
Ni^{2+}	9.89×10^{14}	0.19	(0.17, 0.00)
Fe^{3+}	3.13×10^{14}	0.20	(0.17, 0.02)
Cu^{2+}	1.12×10^{16}	0.13	(0.17, 0.01)
Co^{2+}	6.46×10^{15}	0.12	(0.17, 0.01)

4. *Reference*

[S1] O. Kotova, R. Daly, C.M.G. dos Santos, M. Boese, P.E. Kruger, J.J. Boland and T. Gunnlaugsson, Europium-Directed Self-Assembly of a Luminescent Supramolecular Gel from a Tripodal Terpyridine-Based Ligand, *Angew. Chem. Int. Ed.,* 2012, **51**, 7208–7212.

[S2] K.A. MacGregor, M.J. Robertson, K.A. Young, L. von Kleist, W. Stahlschmidt, A. Whiting, N. Chau, P.J. Robinson, V. Haucke and A. McCluskey, Development of 1,8-Naphthalimides as Clathrin Inhibitors, *J. Med. Chem.,* 2014, **57**, 131–143.

[S3] L.N. Neupane, E.-T. Oh, H.J. Park and K.-H. Lee, Selective and Sensitive Detection of Heavy Metal Ions in 100% Aqueous Solution and Cells with a Fluorescence Chemosensor Based on Peptide Using Aggregation-Induced Emission, *Anal. Chem.,* 2016, **88**, 3333–3340.

[S4] R. Kaushik, A. Ghosh, A. Singh, P. Gupta, A. Mittal and D.A. Jose, Selective Detection of Cyanide in Water and Biological Samples by an Off-the-Shelf Compound, *ACS Sens.,* 2016, **1**, 1265–1271.

[S5] D. F. Sava, L. E. S. Rohwer, M. A. Rodriguez and T. M. Nenoff, Intrinsic Broad-Band White-Light Emission by a Tuned, Corrugated Metal–Organic Framework, *J. Am. Chem. Soc.*, 2012, **134**, 3983–3986.

[S6] N. K. Al-Rasbi, H. Adams and F. O. Suliman, Synthesis, structure and tunable white-light emission of dinuclear Eu(III) Schiff base complex, *Dyes Pigments*, 2014, **104**, 83–88.

[S7] J. Zhang, H. Li, P. Chen, W. Sun, T. Gao and P. Yan, A new strategy for achieving white-light emission of lanthanide complexes: effective control of energy transfer from blue-emissive fluorophore to Eu(III) centres, *J. Mater. Chem. C*, 2015, **3**, 1799–1806.

[S8] R. Boddula, K. Singh, S. Giri and S. Vaidyanathan, Controlled Energy Transfer from a Ligand to an Eu ^{III} Ion: A Unique Strategy To Obtain Bright-White-Light Emission and Its Versatile Applications, *Inorg. Chem.*, 2017, **56**, 10127–10130.

[S9] X.-Q. Song, H.-H. Meng, Z.-G. Lin and L. Wang, 2D Lanthanide Coordination Polymers: Synthesis, Structure, Luminescent Properties, and Ratiometric Sensing Application in the Hydrostable PMMA-Doped Hybrid Films, *ACS Appl. Polym. Mater.*, 2020, **2**, 1644–1655.

[S10] Z. Tang, X. Lyu, L. Luo, Z. Shen and X.-H. Fan, White-Light-Emitting AIE/Eu^{3+}-Doped Ion Gel with Multistimuli-Responsive Properties, *ACS Appl. Mater. Interfaces*, 2020, **12**, 45420–45428.

[S11] J. Chen, Z. Xie, L. Meng, Z. Hu, X. Kuang, Y. Xie and C.-Z. Lu, Luminescence Tunable Europium and Samarium Complexes: Reversible On/Off Switching and White-Light Emission, *Inorg. Chem.*, 2020, **59**, 6963–6977.

[S12] H. Wang, X. Li, H. Cheng, Y.-J. Li, X.-Q. Song and L. Wang, Two luminescent film sensors constructed from new lanthanide coordination polymers for ratiometric detection of Zn^{2+} and NH_3 in water and their white emission properties, *Polym. Chem.*, 2022, **13**, 778–793.

[S13] S. Mund and S. Vaidyanathan, New isomeric ancillary ligands and their Eu^{III} complexes: a single component white light emissive phosphor and their applications in red/white smart LEDs, electronic noses, and temperature sensing, *J. Mater. Chem. C*, 2022, **10**, 7201–7215.

[S14] H.-J. Yu, X.-L. Zhou, X. Dai, F.-F. Shen, Q. Zhou, Y.-M. Zhang, X. Xu and Y. Liu, A tunable full-color lanthanide noncovalent polymer based on cucurbituril-mediated supramolecular dimerization, *Chem. Sci.*, 2022, **13**, 8187–8192.

[S15] A. T. O'Neil, A. Chalard, J. Malmström and J. A. Kitchen, White light and colour-tunable emission from a single component europium-1,8-naphthalimide thin film, *Dalton Trans.*, 2023, **52**, 2255–2261.

[S16] Z. Zhang, N. Ma, S. Yao, W. Han, X. Li, H. Chang and Y.-Y. Wang, Transparent and Hazy Eu_xTb_{1-x} -Nanopaper with Color-Tuning, Photo-Switching, and White Light-Emitting Properties for Anti-counterfeiting and Light-Softened WLEDs, *ACS Sustain. Chem. Eng.*, 2021, **9**, 5827–5837.

[S17] Y. Zhao, F. Zhang, X. Zhang, Single Component Lanthanide Hybrids Based on Metal−Organic Framework for Near-Ultraviolet White Light LED. *ACS Appl. Mater. Interfaces*, 2016, **8**, 24123−24130.

[S18] J. Mao, D. Venugopal, Y. Zhang, P. Zhu and G. Wang, Synthesis and DFT calculation of germanium halide perovskites with high luminescent stability, and their applications in WLEDs and indoor photovoltaics, *Chem. Eng. J.*, 2023, **470**, 144160.

[S19] R. Devi, K. Singh and S. Vaidyanathan, Synergy in the energy transfer between ligands and Eu^{III} ions in molecular europium complexes: single-component white light-emitting luminogens, *J. Mater. Chem. C*, 2020, **8**, 8643–8653.

[S20] J. Wang, Y. Li, X. Li, J. Pan, D. Wang, S. Wei, C. Wang and J. Li, Energy transfer mechanism of carboxymethyl chitosan-Eu^{3+}/Tb^{3+} complex materials and application in multicolor LED, *Carbohydr. Polym.*, 2023, **315**, 120981.

[S21] J. Wang, M. Tai, Z. Yu, S. Kang, D. Jin and L. Wang, Wang, Synthesis and characterization of single-phase Tb^{3+} /Eu^{3+} doped metal–organic framework phosphors for warm light WLED applications, *Dalton Trans.*, 2023, **52**, 1212–1218.

[S22] X. Yu, A. A. Ryadun, K. A. Kovalenko, T. Y. Guselnikova, V. G. Ponomareva, A. S. Potapov and V. P. Fedin, 4 in 1: multifunctional europium–organic frameworks with luminescence sensing properties, white light emission, proton conductivity and reverse acetylene–carbon dioxide adsorption selectivity, *Dalton Trans.*, 2023, **52**, 8695–8703.

[S23] Z. Zhang, Y. Chen, H. Chang, Y. Wang, X. Li and X. Zhu, Aggregation-induced white emission of lanthanide metallopolymer and its coating on cellulose nanopaper for white-light softening, *J. Mater. Chem. C*, 2020, **8**, 2205–2210.

[S24] S. Mund and S. Vaidyanathan, New isomeric ancillary ligands and their Eu^{III} complexes: a single component white light emissive phosphor and their applications in red/white smart LEDs, electronic noses, and temperature sensing, *J. Mater. Chem. C*, 2022, **10**, 7201–7215.

[S25] S. Mund, K. Singh, M. Panda, B. K. Biswal, U. Subuddhi and S. Vaidyanathan, Thiabendazole: a new class of antenna core structure for multifunctional trivalent organo-europium (Eu^{III}) complexes, *J. Mater. Chem. C*, 2022, **10**, 10645–10659.

[S26] Y. Huang, W. Feng, Z. Zhou, H. Zheng, Y. Zhao, H. Yan and X. Lü, Tetraphenylethylene-based Eu^{3+}-metallopolymers with aggregation-enhanced white emission for self-calibrating temperature sensing and white light-emitting diodes (WLEDs), *J. Mater. Chem. C*, 2022, **10**, 7586–7593.

[S27] H. Yu, J. Liu, S. Bao, G. Gao, H. Zhu, P. Zhu and G. Wang, Luminescent lanthanide single atom composite materials: Tunable full-color single phosphor and applications in white LEDs, *Chem. Eng. J.*, 2022, **430**, 132782.

[S28] N. Yang, Z. Zhang, L. Zou, J. Chen, H. Ni, P. Chen, J. Shi and Y. Tong, A novel red-emitting phosphor with an unusual concentration quenching effect for near-UV-based WLEDs, *Inorg. Chem. Front.*, 2022, **9**, 6358–6368.

[S29] Y. Xiang, Z. Liu, Y. Gao, L. Feng, T. Zhou, M. Liu, Y. Zhao, X. Lai, J. Bi and D. Gao, Novel double perovskite $Ca_2Gd_{0.5}Nb_1$-$W_{5/6}O_6$:0.5 Eu^{3+} red phosphors with excellent thermal stability and high color purity for white LEDs, *Chem. Eng. J.*, 2023, **456**, 140901.

[S30] S. Tian, Z. Shi, Y. Sun, P. Zhang, S. Wu, D. Chen, P. Xiong, Q. Qian and Z. Yang, Multicolor Phosphate Glasses for Potential White LED Lighting and X-Ray Detections, *Laser Photonics Rev.*, 2022, **16**, 2200020.

[S31] X. Huang, W. Zhang, X. Wang, J. Zhang, X. Gao and H. Du, Structure and luminescence investigation of Gd^{3+}-sensitized perovskite $CaLa_4Ti_4O_{15}$:Eu^{3+}: A novel red-emitting phosphor for high-performance white light-emitting diodes and plants lighting, *J. Colloid Interface Sci.*, 2022, **608**, 3204–3217.

[S32] Q. Zhang, X. Wang and Y. Wang, A novel germanate based red-emitting phosphor with high efficiency, high color purity and thermal stability for white light-emitting diodes and field emission displays, *Inorg. Chem. Front.*, 2020, **7**, 1034–1045.

[S33] S. U. Khan, W. U. Khan, W. U. Khan, D. Khan, S. Saeed, S. Badshah, M. Ikram and T. A. Saleh, Eu^{3+}, Sm^{3+} Deep-Red Phosphors as Novel Materials for White Light-Emitting Diodes and Simultaneous Performance Enhancement of Organic–

Inorganic Perovskite Solar Cells, *Small*, 2020, **16**, 2001551.

[S34] Y. Bai, Z. Jia, J. Gao, L. Wu, Y. Kong, Y. Zhang and J. Xu, A novel red-emitting phosphor $K_2MgGeO_4:Eu^{3+}$ for WLEDs: zero-thermal quenching induced by heterovalent substitution, *J. Mater. Chem. C*, 2022, **10**, 15957–15966.